

Cosmological simulation with dust formation and destruction

Shohei Aoyama,^{1,2*} Kuan-Chou Hou,^{1,3} Hiroyuki Hirashita,¹ Kentaro Nagamine^{2,4} and Ikkoh Shimizu²

¹*Institute of Astronomy, and Astrophysics, Academia Sinica, PO Box 23-141, Taipei 10617, Taiwan*

²*Theoretical Astrophysics, Department of Earth & Space Science, Osaka University, 1-1 Machikaneyama, Toyonaka, Osaka 560-0043, Japan*

³*Department of Physics & Institute of Astrophysics, National Taiwan University, Taipei 10617, Taiwan*

⁴*Department of Physics & Astronomy, University of Nevada, Las Vegas, 4505 S. Maryland Pkwy, Las Vegas, NV 89154-4002, USA*

Accepted XXX. Received YYY; in original form ZZZ

ABSTRACT

To investigate the evolution of dust in a cosmological volume, we perform hydrodynamic simulations, in which the enrichment of metals and dust is treated self-consistently with star formation and stellar feedback. We consider dust evolution driven by dust production in stellar ejecta, dust destruction by sputtering, grain growth by accretion and coagulation, and grain disruption by shattering, and treat small and large grains separately to trace the grain size distribution. After confirming that our model nicely reproduces the observed relation between dust-to-gas ratio and metallicity for nearby galaxies, we concentrate on the dust abundance over the cosmological volume in this paper. The comoving dust mass density has a peak at redshift $z \sim 1-2$, coincident with the observationally suggested dustiest epoch in the Universe. In the local Universe, roughly 10 per cent of the dust is contained in the intergalactic medium (IGM), where only 1/3–1/4 of the dust survives against dust destruction by sputtering. We also show that the dust mass function is roughly reproduced at $\lesssim 10^8 M_{\odot}$, while the massive end still has a discrepancy, which indicates the necessity of stronger feedback in massive galaxies. In addition, our model broadly reproduces the observed radial profile of dust surface density in the circum-galactic medium (CGM). While our model satisfies the observational constraints for the dust extinction on cosmological scales, it predicts that the dust in the CGM and IGM is dominated by large ($> 0.03 \mu\text{m}$) grains, which is in tension with the steep reddening curves observed in the CGM.

Key words: dust, extinction – methods: numerical – ISM: dust – galaxies: evolution – galaxies: formation – galaxies: ISM

1 INTRODUCTION

Dust is an essential component in understanding star formation properties of galaxies both observationally and theoretically. Because dust absorbs stellar ultraviolet (UV)–optical light and reemits it in the infrared (IR) (e.g. Calzetti et al. 2000; Buat et al. 2002; Takeuchi et al. 2012), a precise estimation of star formation rate (SFR) in galaxies requires correction for dust extinction (e.g. Steidel et al. 1999; Takeuchi et al. 2010; Kennicutt & Evans 2012). The analysis of Takeuchi et al. (2005) revealed that a higher fraction of star formation is hidden by dust at $z \sim 1$ than at $z \sim 0$, where z is the redshift, and that more than half of the star

formation activity is enshrouded by dust at $0.5 \leq z \leq 1.2$ (see also Burgarella et al. (2013) and references therein).

There are some interesting theoretical issues in which dust plays a significant role. Dust is an efficient catalyst of molecular hydrogen (H_2) formation in the interstellar medium (ISM) (e.g. Gould & Salpeter 1963; Cazaux & Tielens 2004; Cazaux & Spaans 2009). Hirashita & Ferrara (2002) showed that early dust production at high redshift dramatically enhances the H_2 abundance, which probably leads to an enhancement of star formation activity in galaxies. Dust has an impact on gas dynamics in dusty clouds through radiation pressure (e.g. Ishiki & Okamoto 2017, for a recent development). In addition, the typical mass of the final fragments in star-forming clouds is also regulated by dust cool-

* E-mail: saoyama@asiaa.sinica.edu.tw (SA)

ing (Whitworth et al. 1998; Omukai 2000; Larson 2005; Omukai et al. 2005; Schneider et al. 2006); this effect could have a dramatic impact on the stellar initial mass function. Moreover dust eventually becomes the ingredient of planets in protostellar discs.

The evolution of the total dust amount in a galaxy can be broadly understood in the chemical evolution framework since dust evolution is strongly linked to metal enrichment (Lisenfeld & Ferrara 1998; Mattsson et al. 2014). As shown in a variety of chemical evolution models, the increase of the dust amount is mainly driven by dust condensation in stellar ejecta and dust growth in the dense ISM, while the decrease occurs when the dust is swept by supernova (SN) shocks (Dwek 1998; Zhukovska et al. 2008; Calura et al. 2008; Inoue 2011; Hirashita & Kuo 2011; Asano et al. 2013a; Gioannini et al. 2017). When we consider the property of dust grains in the ISM, not only the total dust abundance but also the grain size distribution is of fundamental importance (e.g. Mathis et al. 1977; Nozawa & Fukugita 2013). In particular, the extinction curve (i.e. the wavelength dependence of absorption and scattering cross-section) depends sensitively on the grain size distribution (Bohren et al. 1983; Hou et al. 2017). In addition, the total grain surface area, which depends on the grain size distribution, governs the rate of grain-surface H_2 formation (Barlow & Silk 1976; Yamasawa et al. 2011).

Dust evolution is driven by the interactions not only with gas particles but also with dust itself in the ISM (see Asano et al. 2013b, and references therein for the processes described in what follows). Dust grains are produced by SNe and asymptotic giant branch (AGB) stars, and after being injected into the ISM, they suffer destruction in SN shocks sweeping the ISM. Dust grains grow by accreting surrounding gas-phase metals in the dense ISM. Dust grains interact with themselves via collisional processes such as coagulation and shattering. The rates of the above grain processing mechanisms in the ISM (dust destruction, accretion, coagulation, and shattering) depend not only on the local physical condition of the gas but also on the dust abundance and metallicity. Moreover, as found by Kuo & Hirashita (2012), the efficiency of interstellar processing could depend strongly on the grain size distribution. Therefore, for a complete understanding of dust evolution, we must consider not only the evolution of dust abundance but also that of grain size distribution.

Asano et al. (2013b) constructed a full framework for treating the evolution of grain size distribution consistently with the enrichment of metals and dust in a galaxy. They treated all the above processes of dust evolution and revealed that all of these processes are necessary for a comprehensive understanding of the observed dust-to-gas mass ratios and extinction curves in nearby galaxies (see Nozawa et al. 2015 for an extension of their model to high redshift). To focus on the dust evolution, they treated a galaxy as a one-zone object. As a consequence of their modelling, they succeeded in providing a tool to understand not only observed gas-to-dust mass ratios but also extinction curves in galaxies (Asano et al. 2014).

Since the dust evolution is affected by the physical condition of the ISM where it resides, it is important to deeply understand the hydrodynamical evolution of the ISM in a spatially resolved way. Hydrodynamical simulations have

indeed been a powerful tool to clarify galaxy formation and evolution. They provide a significant advantage over simple one-zone calculations, which generally need to introduce some strong assumptions such as instantaneous mixing and homogeneity. Many cosmological hydrodynamic simulations have reproduced and predicted the observed galaxy mass and luminosity functions (e.g. Nagamine et al. 2001, 2004; Choi & Nagamine 2012; Jaacks et al. 2012, 2013; Shimizu et al. 2014; Thompson et al. 2014; Vogelsberger et al. 2014; Shimizu et al. 2016; Schaye et al. 2015; Schaller et al. 2015; Duffy et al. 2017; McCarthy et al. 2017; Pillepich et al. 2018). There have been some attempts to include dust evolution in cosmological hydrodynamical simulations. Dayal et al. (2010) calculated dust formation and destruction by SNe in their cosmological simulation and predicted the submillimetre fluxes from high-redshift Lyman break galaxies. Yajima et al. (2015) calculated the radiation transfer of UV light based on the spatial distribution of metals in their zoom-in simulations, and estimated the IR luminosities of individual high- z galaxies. They assumed a constant dust-to-metal ratio, and did not explicitly treat the dust evolution.

Bekki (2013a,b, 2015) treated dust as a separate component from gas, dark matter and star particles and solved the interaction between dust and gas. They calculated H_2 formation on dust surfaces and dust evolution consistently to investigate the spatial distribution of dust and molecular gas in galaxies. McKinnon et al. (2016) traced dust evolution along with the hydrodynamical evolution of the gas by performing cosmological zoom-in simulations. They revealed the importance of dust growth by accretion, and pointed out the necessity of a more realistic treatment of dust destruction and feedback by SNe. In addition, McKinnon et al. (2017) compared statistical properties of dust, especially, the dust mass function and the comoving dust mass density, and found that their simulation broadly reproduced the observation in the present-day Universe, although it tended to underestimate the dust abundance in high- z dusty galaxies. Zhukovska et al. (2016) analyzed dust evolution in an isolated Milky Way-like galaxy by post-processing the simulation of Dobbs & Pringle (2013). They put particular focus on dust growth by accretion and examined gas-temperature-dependent sticking coefficient in accretion, in order to reproduce the relation between silicon depletion and gas density.

All these simulations only traced the dust abundance, but did not treat the grain size distribution. As mentioned above, the grain size distribution affects the dust evolution. For the grain size distribution, in addition to the processes included in the above simulations, shattering and coagulation are important. Implementation of grain size distributions in hydrodynamical simulations has not been successful, mainly because of the high computational cost. Calculating the grain size distribution in a fully self-consistent manner over the cosmic age is computationally expensive even in one-zone calculation as shown by Asano et al. (2013b). Recently, McKinnon et al. (2018) implemented a full grain size distribution in their hydrodynamical simulation. However their simulation is still limited to an isolated galaxy. For the purpose of treating the evolution of grain size distribution within the available computational capability, Aoyama et al. (2017, hereafter A17) and Hou et al. (2017) adopt the two-size approximation formulated by Hirashita (2015), in which

the entire grain size range is represented by two size ranges divided at around $a \approx 0.03\mu\text{m}$ (a is the grain radius). Hirashita (2015) confirmed that the two-size approximation gives the same evolutionary behavior of grain size distribution and extinction curve as calculated by the full treatment of Asano et al. (2013b, 2014). Because this two-size approximation reduces the computational cost, it provides a feasible way to compute the evolution of grain size evolution in hydrodynamical simulations. Consequently, we can not only compute the spatial variations in dust abundance, but also examine the grain size distribution as a function of time and metallicity.

The hydrodynamical simulation in A17, Hou et al. (2017) and Gjergo et al. (2018) treated the dust evolution using the two size approximation in a consistent manner with the local physical states such as the local gas density and temperature. They succeeded in theoretically predicting spatial inhomogeneity in the dust abundance (A17), extinction curves (Hou et al. 2017) and the relation between dust-to-gas mass ratio and oxygen abundance (Gjergo et al. 2018). However, in A17 and Hou et al. (2017), only a single isolated spiral galaxy was simulated. Gjergo et al. (2018) performed zoom-in simulations and analyzed only four massive clusters. Therefore no statistical information on dusty galaxies was achievable.

In order to obtain general evolutionary features of galaxies, a simulation on a cosmological spatial scale and time-scale is desired. Such a cosmological simulation is capable of predicting the evolution of a large number of galaxies. McKinnon et al. (2016, 2017) implemented dust evolution in a cosmological hydrodynamic simulation, and succeeded in predicting statistical properties of galaxies such as the dust mass function and the scaling relations of dust abundance with quantities characterizing galaxies. However, they did not include the evolution of grain size distribution. As mentioned above, the evolution of grain size distribution is of fundamental importance in understanding the dust evolution.

Another important point of cosmological simulations is that they are able to predict the dust and metal enrichment of the intergalactic medium (IGM). Ménard et al. (2010) observationally revealed that dust grains are sure to exist in the circumgalactic medium (CGM) and IGM. The CGM is defined as the medium located from \gtrsim a few tens of kpc to ~ 1 Mpc from the galaxy centre (Ménard et al. 2010). Ménard & Fukugita (2012) estimated the abundance and radial profile of dust in the CGM using Mg II absorbers as tracers. On the theoretical side, Inoue & Kamaya (2003) showed that dust grains in the IGM affect the thermal history of the IGM through photoelectric heating. They also pointed out that the efficiency of photoelectric heating depends on the grain size. Therefore, clarifying the evolution of dust abundance and grain size distribution in the IGM is important. In addition, Nagamine et al. (2016) and Zu et al. (2011) mention that the metal distribution in the IGM is sensitive to feedback (energy injection) models. Because dust grains are created by metal condensation and spread to the ISM and the IGM in a way dependent on the feedback strength (Hou et al. 2017), the distribution of dust grains could also be useful for testing feedback models.

In this paper, we perform cosmological N -body/SPH simulations with GADGET3-OSAKA developed in A17 based

Table 1. Simulation setup

Name	Boxsize [h^{-1} Mpc]	N	$\varepsilon_{\text{grav}}$ [h^{-1} kpc]	m_{dm} [$h^{-1} M_{\odot}$]	$m_{\text{gas}}^{\text{init}}$ [$h^{-1} M_{\odot}$]
L50N512	50	2×512^3	3	6.89×10^7	1.28×10^7
L50N256	50	2×256^3	5	5.51×10^8	1.02×10^8

Notes. N , $\varepsilon_{\text{grav}}$, m_{dm} and $m_{\text{gas}}^{\text{init}}$ are the number of particles, the gravitational softening length, the mass of dark matter particle and the initial mass of gas particle, respectively.

on the original GADGET code (Springel 2005). In this paper, we particularly focus on the overall dust properties in a cosmological volume. We also test the statistical properties of the dust content in galaxies, and examine the dust enrichment in the IGM as a result of cosmic structure formation and SN feedback. The cosmic history of dust enrichment and the evolution of grain size distribution on a cosmological spatial scale and time-scale are the main topics of this paper. The detailed analysis of individual galaxies is described in a separate paper (Hou et al., in preparation).

This paper is organized as follows. In Section 2, we explain the model of dust evolution in the cosmological simulation. We present the simulation results in Section 3. We discuss the parameter dependence in Section 4. We conclude in Section 5. Throughout this paper, we adopt $Z_{\odot} = 0.02$ for the solar metallicity following Hirashita (2015). This value, used as simple metallicity normalization, does not affect our main results. We adopt the following cosmological parameters (Planck Collaboration et al. 2016): baryon density parameter $\Omega_{\text{b}} = 0.049$, total matter density parameter $\Omega_{\text{m}} = 0.32$, cosmological constant parameter $\Omega_{\Lambda} = 0.68$, Hubble constant $H_0 = 67 \text{ km s}^{-1} \text{ Mpc}^{-1}$, power spectrum index $n_{\text{s}} = 0.9645$, and density fluctuation normalization $\sigma_8 = 0.831$. In this paper, we also use $h \equiv H_0/(100 \text{ km s}^{-1} \text{ Mpc}^{-1}) = 0.67$ for the non-dimensional Hubble constant.

2 MODEL

2.1 Galaxy evolution simulation

We basically use the same simulation code as used in A17 (GADGET3-OSAKA) but we perform a cosmological simulation. We generated initial conditions at $z = 99$ with MUSIC (Hahn & Abel 2011). The basic features in the simulation other than dust implementation are described in a separate paper (Shimizu et al., in preparation). Below we explain our simulation focusing on the difference from A17. We performed cosmological hydrodynamical simulations with a comoving $50h^{-1}$ Mpc box. The initial number of particles are 2×256^3 and 2×512^3 (referred to as L50N256 and L50N512, respectively). Other parameters of simulations are shown in Table 1.

In our simulation, stars are formed in dense and cold gas particles. Star particles are created from gas particles whose number density is greater than $n_{\text{th}} = 0.1 \text{ cm}^{-3}$ and temperature is less than $T_{\text{th}} = 10^4 \text{ K}$ with the following SFR:

$$\frac{d\rho_*}{dt} = \varepsilon_* \frac{\rho_{\text{gas}}}{t_{\text{ff}}}, \quad (1)$$

where ρ_* and ρ_{gas} are the local mass density of newly formed

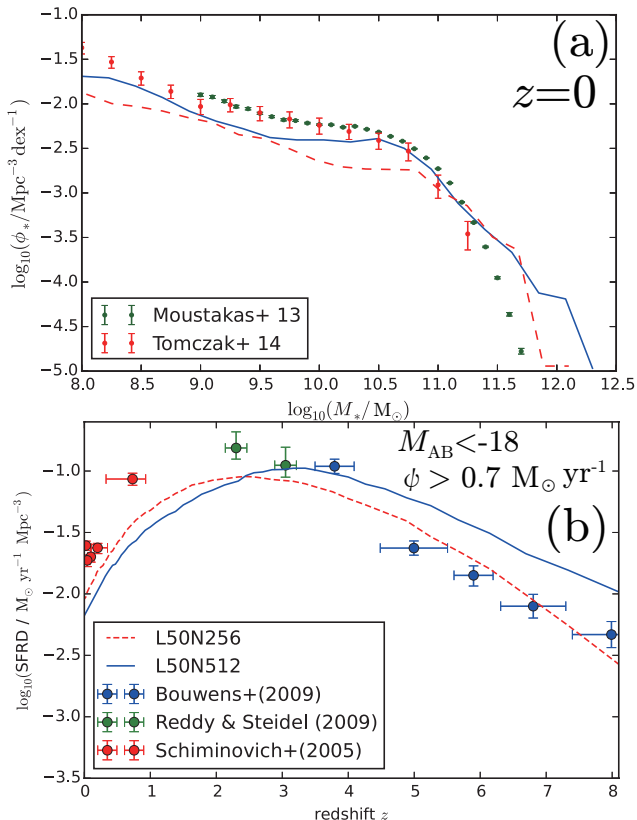


Figure 1. (a) Stellar mass function at $z = 0$ for L50N512 (blue solid line) and L50N256 (red dashed line) (see Table 1 for these two simulations). The observational data are taken from Moustakas et al. (2013) and Tomczak et al. (2014) as shown in the legend. (b) Cosmic star formation rate density (SFRD) with L50N512 (blue solid line) and L50N256 (red dashed line). They are shown with observational data based on far-UV galaxy samples (Schiminovich et al. 2005) and Lyman break galaxies (Bouwens et al. 2009; Reddy & Steidel 2009). Taking the observational detection limits into account, we only consider the galaxies with star formation rate $\psi > 0.7 M_{\odot} \text{ yr}^{-1}$ (corresponding to the absolute AB magnitude $M_{\text{AB}} < -18$ according to the conversion formula in Madau et al. (1998)) for a fair comparison.

stars and gas, respectively, ε_* is the star formation efficiency in a free-fall time (we adopt $\varepsilon_* = 0.05$ in this paper), and $t_{\text{ff}} \equiv \sqrt{3\pi/(32G\rho_{\text{gas}})}$ is the local free-fall time. The temperature threshold is used to search a region where Lyman α cooling has made a favourable condition for gas collapse (or star formation) (e.g. Sutherland & Dopita 1993). The threshold density is determined by the extrapolation of so-called Larson’s law (Larson 1981) to our spatial resolution (~ 1 kpc): this density criterion serves to choose regions where bound objects like molecular clouds are potentially formed. We also confirmed that the resulting SFR is roughly consistent with the Schmidt–Kennicutt law in isolated galaxies (Shimizu et al., in preparation). We include the metal and dust production by not only Type II SNe but also Type Ia SNe and AGB stars. The formation of various heavy elements is treated by implementing the CELib package (Saitoh 2017) to GADGET3-OSAKA. Energy input from massive stars (stellar feedback) is also considered.

The model is successful in reproducing the main

statistical properties of star formation and stellar content in galaxies, especially, the cosmic star formation rate density (SFRD) and the stellar mass function at $z = 0$ (Schiminovich et al. 2005; Bouwens et al. 2009; Reddy & Steidel 2009; Moustakas et al. 2013; Tomczak et al. 2014), except at the very massive end of the stellar mass function, as shown in Fig. 1. Comparing the results of L50N512 and L50N256, we find that the stellar mass function and the SFRD at low- z ($z \lesssim 3$) do not significantly depend on the mass resolution. However the SFRD at high z ($z \gtrsim 3$) does depend on the mass resolution, because more low-mass galaxies can form in a higher resolution simulation.

Feedback of active galactic nuclei (AGN) is not included to avoid further complexity not related to dust production, although it might resolve the discrepancy in the stellar mass function at the very massive end. AGN feedback has been implemented in many cosmological simulations and shown to be responsible for suppressing the formation of massive objects (e.g. Vogelsberger et al. 2013, 2014; Sijacki et al. 2015; Weinberger et al. 2017; Fiacconi et al. 2018). However, the treatment of AGN feedback depends on subgrid models, which involve choice of model parameters (e.g. Vogelsberger et al. 2013). In addition, AGN feedback is also related to the formation of supermassive black holes. Although the relation between growth of supermassive black hole and dust enrichment is an interesting topic (Valiante et al. 2011), we choose to focus on the processes directly related to dust formation in this paper. Therefore, we leave the influence of AGN feedback for the future work.

2.2 Basic treatment of dust evolution

In this paper, we basically adopt the dust evolution model used in our previous isolated-galaxy simulation (A17; Hou et al. 2017). We represent the whole range of grain radii by large and small grain populations roughly separated at $a \sim 0.03 \mu\text{m}$ according to Hirashita (2015). We set the typical radii of the large and small grain populations as $0.1 \mu\text{m}$ and $5 \times 10^{-3} \mu\text{m}$, respectively.

The abundances of the two dust populations on a gas particle are represented by the dust-to-gas mass ratios, \mathcal{D}_{L} and \mathcal{D}_{S} , as

$$\mathcal{D}_{\text{L}} = \frac{m_{\text{L}}}{m_{\text{g}}}, \quad (2)$$

$$\mathcal{D}_{\text{S}} = \frac{m_{\text{S}}}{m_{\text{g}}}, \quad (3)$$

where m_{g} is the mass of the gas particle, and m_{L} and m_{S} are the total mass of large and small grains in the gas particle, respectively. Hereafter, we refer to \mathcal{D}_{L} (\mathcal{D}_{S}) as the large (small) grain abundance. The total dust-to-gas ratio \mathcal{D}_{tot} is defined as

$$\mathcal{D}_{\text{tot}} \equiv \mathcal{D}_{\text{L}} + \mathcal{D}_{\text{S}}. \quad (4)$$

In our simulation, each gas particle has its own dust abundance $\mathcal{D}_{\text{L}(i)}$ and $\mathcal{D}_{\text{S}(i)}$, where suffix (i) indicates the label for the gas particle. Based on the two-size model, we calculate the formation and destruction of large and small dust grains on each gas particle using variables and outputs in the simulation as described below (see A17, especially their equations 13 and 14 for further details).

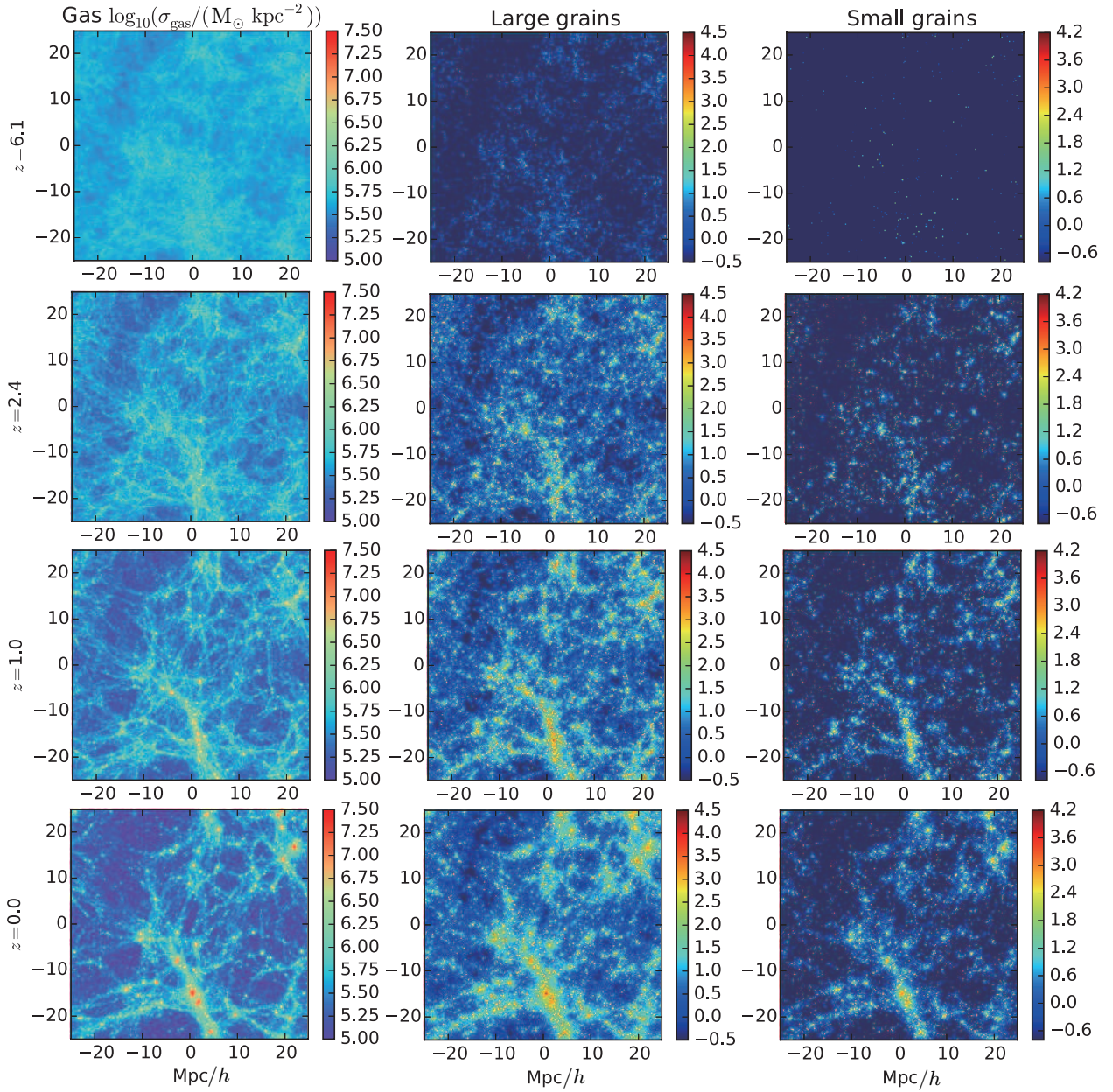


Figure 2. Time evolution of the projected density field ($\int \rho(\mathbf{x}) dz$) of gas and small and large grains at $z = 6.1, 2.4, 1.0, 0.0$, where $\rho(\mathbf{x})$ is the density at position \mathbf{x} of each component. The depth of the integration is $50 h^{-1} \text{Mpc}$. The comoving box size is $50 h^{-1} \text{Mpc}$ and the colour indicates the log-scale density of each component in units of $M_{\odot} \text{kpc}^{-2}$ (shown by the colour bar).

We calculate the time evolution of the large and small grain abundances in the i -th particle at time t as (Appendix

$$\begin{aligned}
 \text{A)} \quad \frac{d\mathcal{D}_{L(i)}(t)}{dt} &= - \left(\frac{\mathcal{D}_{L(i)}(t)}{\tau_{\text{sh}}} - \frac{\mathcal{D}_{S(i)}(t)}{\tau_{\text{co}}} \right) - \frac{\mathcal{D}_{L(i)}(t)}{\tau_{\text{sp}}(a_L)} \\
 &+ \left[\frac{d\mathcal{D}_{L(i)}(t)}{dt} \right]_{\text{Source}} - \left[\frac{d\mathcal{D}_{L(i)}(t)}{dt} \right]_{\text{SNe}} \\
 &- \frac{\mathcal{D}_{L(i)}(t)}{m_{g(i)}} \frac{dm_{g(i)}^{\text{return}}}{dt}, \quad (5)
 \end{aligned}$$

$$\begin{aligned}
 \frac{d\mathcal{D}_{S(i)}(t)}{dt} &= \left(\frac{\mathcal{D}_{L(i)}(t)}{\tau_{\text{sh}}} - \frac{\mathcal{D}_{S(i)}(t)}{\tau_{\text{co}}} + \frac{\mathcal{D}_{S(i)}(t)}{\tau_{\text{acc}}} \right) \\
 &- \frac{\mathcal{D}_{S(i)}(t)}{\tau_{\text{sp}}(a_S)} - \left[\frac{d\mathcal{D}_{S(i)}(t)}{dt} \right]_{\text{SNe}} \\
 &- \frac{\mathcal{D}_{S(i)}(t)}{m_{g(i)}} \frac{dm_{g(i)}^{\text{return}}}{dt}, \quad (6)
 \end{aligned}$$

where τ_{sh} , τ_{co} , and τ_{acc} are the time-scales of shattering, coagulation, and accretion, respectively, and $dm_{\text{g}(i)}^{\text{return}}/dt$ is the gas ejection rate from stars (note that the ejected gas dilutes the dust-to-gas ratio).¹ The parameter $\tau_{\text{sp}}(a)$ is the sputtering time-scale as a function of grain radius in the hot gas not associated with SNe (see Section 2.3), and the terms with ‘Source’ and ‘SNe’ describe the stellar dust production and SN destruction, respectively. In our formulation, these time-scales depend on the gas density, dust abundances, and/or metallicity but the dependence on those quantities are not explicitly shown here for the brevity of notation. The formation and destruction terms are evaluated by

$$\left[\frac{d\Delta\mathcal{D}_{L(i)}(t)}{dt} \right]_{\text{Source}} dt = f_{\text{in}} \frac{\Delta m_{\text{metal}}}{m_{\text{g}(i)}} (1 - \delta), \quad (7)$$

$$\left[\frac{d\Delta\mathcal{D}_{L,S(i)}(t)}{dt} \right]_{\text{SNe}} dt = \left[1 - (1 - \eta)^{N_{\text{SN}}} \right] \mathcal{D}_{S/L(i)}(t), \quad (8)$$

where f_{in} is the dust condensation efficiency of metals in the stellar ejecta (we assume $f_{\text{in}} = 0.1$ following A17), Δm_{metal} is the ejected metal mass from stars, δ is the destroyed fraction of newly formed dust, N_{SNe} is the number of SNe that affect the gas particle of interest (note that, because a star particle represents a cluster of $\sim 10^6$ – 10^7 stars and contains a number of massive stars, a number of SNe are treated as a single explosion from the star particle), and η is the destroyed fraction of preexisting dust by a single SN (see the evaluations of δ , N_{SNe} and η in A17).²

The time-scale parameters of accretion, coagulation, and shattering are determined in the following way (see A17 and references therein for the detailed derivation). Since accretion and coagulation occur in the dense clouds, which cannot be resolved in our simulations, we adopt a subgrid model. We assume that dense ($n_{\text{gas}} > 1 \text{ cm}^{-3}$, where n_{gas} is the gas number density) and cold gas particles ($T_{\text{gas}} < 10^4 \text{ K}$, where T_{gas} is the gas temperature), which are referred to as the *dense gas particles*, host dense clouds with 50 K and 10^3 cm^{-3} . Because the cosmological simulations in this paper only resolve less dense gas than the single-galaxy simulation in A17, we apply a looser condition for the identification of the dense gas particles. We assume that the dense clouds occupy a mass fraction of $f_{\text{dense}} = 0.1$ in the dense gas particles (see Section 2.3 of A17 for the definition of f_{dense}). Accretion and coagulation are assumed to occur only in the dense gas particles. The time-scales of accretion and coagulation (τ_{acc} and τ_{co}) are evaluated as follows:

$$\tau_{\text{acc}} = \begin{cases} 1.2 \times 10^6 \text{ yr} \left(\frac{Z}{Z_{\odot}} \right)^{-1} \left(1 - \frac{\mathcal{D}_{\text{tot}}}{Z} \right)^{-1} / f_{\text{dense}} \\ \quad \text{(in dense gas particles)}, \\ \infty \text{ (otherwise)}, \end{cases} \quad (9)$$

¹ Equations (13) and (14) in A17 need to be corrected by including this dilution term. However, A17 correctly included this term in their code and calculations.

² In A17, their equation (19) corresponding equation (8) used a notation of $\mathcal{D}_{(\text{SNe}/L,S)(i)}(t)$, which should be simply $\mathcal{D}_{S/L(i)}(t)$.

$$\tau_{\text{co}} = \begin{cases} 2.71 \times 10^5 \text{ yr} \left(\frac{\mathcal{D}_{\text{S}}}{0.01} \right)^{-1} \left(\frac{v_{\text{co}}}{0.1 \text{ km s}^{-1}} \right)^{-1} / f_{\text{dense}} \\ \quad \text{(in dense gas particles)}, \\ \infty \text{ (otherwise)}, \end{cases} \quad (10)$$

where Z is the metallicity of the gas particle. Shattering is assumed to occur only in the diffuse gas whose number density is smaller than 1 cm^{-3} :

$$\tau_{\text{sh}} = \begin{cases} 5.41 \times 10^7 \text{ yr} \left(\frac{\mathcal{D}_{\text{L}}}{0.01} \right)^{-1} \left(\frac{n_{\text{gas}}}{1 \text{ cm}^{-3}} \right)^{-1} \\ \quad (n_{\text{gas}} < 1 \text{ cm}^{-3}), \\ \infty (n_{\text{gas}} \geq 1 \text{ cm}^{-3}). \end{cases} \quad (11)$$

2.3 Sputtering not directly associated with SNe

The sputtering terms in equations (5) and (6) were not included in our previous model (A17). Dust grains are destroyed by sputtering in high-temperature ($\gtrsim 10^6 \text{ K}$) regions such as X-ray-emitting hot gas in the CGM or IGM (Tsai & Mathews 1995). Note that we have already counted the dust destruction in SN shocks. Thus, to avoid double-counting the destruction, we extract the diffuse hot gas not associated with SNe by imposing the density threshold for sputtering at $n_{\text{th}}^{\text{sp}} = 0.01 \text{ cm}^{-3}$, and consider the dust destruction by sputtering only in regions with $n_{\text{gas}} < n_{\text{th}}^{\text{sp}}$ and $T > 10^6 \text{ K}$. We adopt the following destruction time-scale based on Tsai & Mathews (1995) (see also Draine & Salpeter 1979; Nozawa et al. 2006; Hirashita et al. 2015):

$$\tau_{\text{sp}}(a, n_{\text{H}}) = \begin{cases} 2.1 \times 10^5 \left(\frac{a}{1 \mu\text{m}} \right) \left(\frac{n_{\text{gas}}}{1 \text{ cm}^{-3}} \right)^{-1} \\ \quad \text{(if } n_{\text{gas}} < n_{\text{th}}^{\text{sp}} \text{ and } T_{\text{gas}} > 10^6 \text{ K)}, \\ \infty \text{ otherwise.} \end{cases} \quad (12)$$

where n_{H} is the hydrogen number density.

2.4 Time-step for dust treatment

Some of the time-scales concerning dust evolution processes could be shorter than the hydrodynamical time-step adopted in the GADGET-3 code (Springel et al. 2001a). In this case, we calculate the dust evolution by dividing a single hydrodynamical time-step into multiple sub-cycles. We set the sub-cycle time-step Δt_{sub} as follows:

$$\Delta t_{\text{sub}} = \varepsilon_{\text{sub}} \left[\max \left(\tau_{\text{hydro}}^{-1}, \tau_{\text{acc}}^{-1}, \tau_{\text{sh}}^{-1}, \tau_{\text{co}}^{-1} \right) \right]^{-1}, \quad (13)$$

where ε_{sub} is a constant which controls the accuracy of the calculation. Because we use the fourth-order classical Runge-Kutta method for the dust evolution, the error of time integration should be suppressed as $\propto \varepsilon_{\text{sub}}^4$. In this paper, we set $\varepsilon_{\text{sub}} = 0.1$.

2.5 Galaxy identification and definition of the IGM

We analyze the dust associated with galaxies and that contained in the IGM separately. In order to distinguish between these two regions, we identify galaxies, and define the intergalactic space as the regions not associated with the

galaxies. In order to identify galaxies in a simulation snapshot, we use P-STAR GROUPEFINDER (Springel et al. 2001b). In what follows, we give a brief summary of the algorithm following Nagamine et al. (2004). First, the baryonic (gas + stars) density peaks in the smoothed density field are identified. Second, the densities of N_{ngb} nearest neighbor particles around the density peak are measured, and the peak-density particle is considered as a ‘head particle’ if all the neighbor particles have lower densities. In this paper, we adopt $N_{\text{ngb}} = 128$ and 512 for L50N256 and L50N512, respectively. Finally, the gas and star particles near the head particle above a density threshold described by Nagamine et al. (2004) are grouped and identified as a galaxy. In our definition, we identify the objects whose stellar mass is greater than $10^8 M_{\odot}$ as galaxies, since the smaller structures are affected by our finite mass resolution. The IGM is defined as the medium not belonging to the galaxies identified above.

3 RESULTS

First, we test if the dust enrichment is successfully implemented by comparing our theoretical prediction to the observed dust abundance at $z = 0$, where the relation between dust abundance and metallicity is well studied. As mentioned in the Introduction, we focus on the dust properties in galaxies, the CGM and the IGM. Second, we present the evolution of the cosmic dust abundance. In particular, we predict the grain size distribution (i.e. small/large grain abundance) in a cosmological volume for the first time. We also show the dust mass function of galaxies and present the radial profile of dust mass around massive galaxies in the CGM. Finally, we show the cosmic extinction (extinction on cosmological scales) and compare it with the corresponding observational results.

3.1 Relation between dust abundance and metallicity

Because dust production is strongly associated with metal enrichment, the relation between dust abundance and metallicity gives a strong test for dust evolution models (Lisenfeld & Ferrara 1998; Dwek 1998). Some cosmological modeling with dust implementation also uses this relation for a critical test (Popping et al. 2017; Ginolfi et al. 2018). We show the galaxy distribution on the $\mathcal{D}_{\text{tot}}-Z$ (total dust-to-gas ratio vs. metallicity) diagram at $z = 0$ in Fig. 3. Each point indicates an individual galaxy and its colour indicates the total stellar mass (M_*). We observe in Fig. 3 that the metallicity and dust abundance are low for $M_* \lesssim 10^{8.5} M_{\odot}$. If the metallicity is low, dust growth by accretion is not efficient, so that the major part of dust is produced by stellar sources. Thus, the dust-to-gas ratio follows $\mathcal{D}_{\text{tot}} \approx f_{\text{in}}Z$ for low-mass galaxies.

In the middle mass range $10^{8.5} M_{\odot} \lesssim M_* \lesssim 10^{10} M_{\odot}$, \mathcal{D}_{tot} increases steeply at $Z \gtrsim 0.1Z_{\odot}$. In these galaxies, star formation occurs continuously and metal enrichment proceeds. As a consequence, dust growth by accretion occurs and the dust-to-gas ratio increases steeply. The relation between dust-to-gas ratio and metallicity in this galaxy mass range is also consistent with the observational trend in

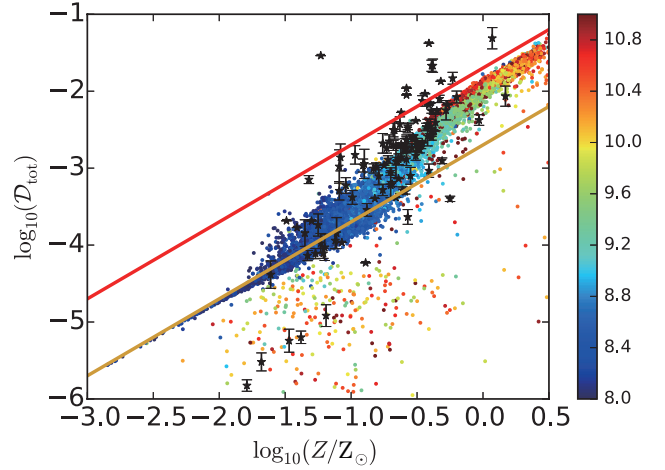


Figure 3. Relation between dust-to-gas mass ratio (\mathcal{D}_{tot}) and metallicity Z of individual galaxies. The color indicates the logarithmic stellar mass (M_{\odot}). The yellow and red lines represent the linear relation of the stellar yield ($\mathcal{D}_{\text{tot}} = f_{\text{in}}Z$) and the saturation limit ($\mathcal{D}_{\text{tot}} = Z$), respectively. The black stars denote the observational result which was reported by Rémy-Ruyer et al. (2014).

a nearby star-forming galaxy sample in Rémy-Ruyer et al. (2014).

At the massive end, $M \gtrsim 10^{10} M_{\odot}$, where the metallicity is high, dust growth by accretion is saturated because of the limit $\mathcal{D}_{\text{tot}} \leq Z$. The $\mathcal{D}_{\text{tot}}-Z$ relation of the simulated high-metallicity galaxies lies within the dispersion of the observational data points. Some observational data are in the area of $\mathcal{D}_{\text{tot}} > Z$, which is unphysical. There could still be a significant uncertainty in the observational dust mass estimate.

In our simulation, there are some outliers located far below the line of $\mathcal{D}_{\text{tot}} = f_{\text{in}}Z$. In our model, such an extremely low dust-to-metal ratio can only be produced by SN destruction. Interestingly, some observational data points also show such an extremely low dust-to-metal ratio. However, we emphasize that those outliers account for a tiny fraction of the entire galaxy population in our model, and that most of the galaxies show a clear correlation between dust-to-gas ratio and metallicity.

3.2 Cosmic dust abundance

We show the evolution of the cosmic dust density normalized to the critical density of the Universe, i.e. $\Omega_{\text{dust}}(z)$ in Fig. 4. We also separately show the dust abundances in galaxies and the IGM based on the galaxy identification explained in Section 2.5; that is, we sum up all the dust mass contained in galaxies and subtract it from the total dust mass to obtain the IGM dust abundance. To specify each component, we put superscript ‘L’ and ‘S’ for large and small grains, respectively, no superscript for the total dust abundance, and subscript ‘gal’ and ‘IGM’ for dust in the galaxies and the IGM, respectively. For example, $\Omega_{\text{dust,IGM}}^{\text{L}}$ and $\Omega_{\text{dust,IGM}}^{\text{S}}$ mean the comoving density of large and small grains in IGM, respectively, and $\Omega_{\text{dust,IGM}} = \Omega_{\text{dust,IGM}}^{\text{S}} + \Omega_{\text{dust,IGM}}^{\text{L}}$.

Galaxies are enriched with dust through stellar dust production and dust growth by accretion. Star formation starts at $z \sim 15$ in our simulation. Dust in galaxies contin-

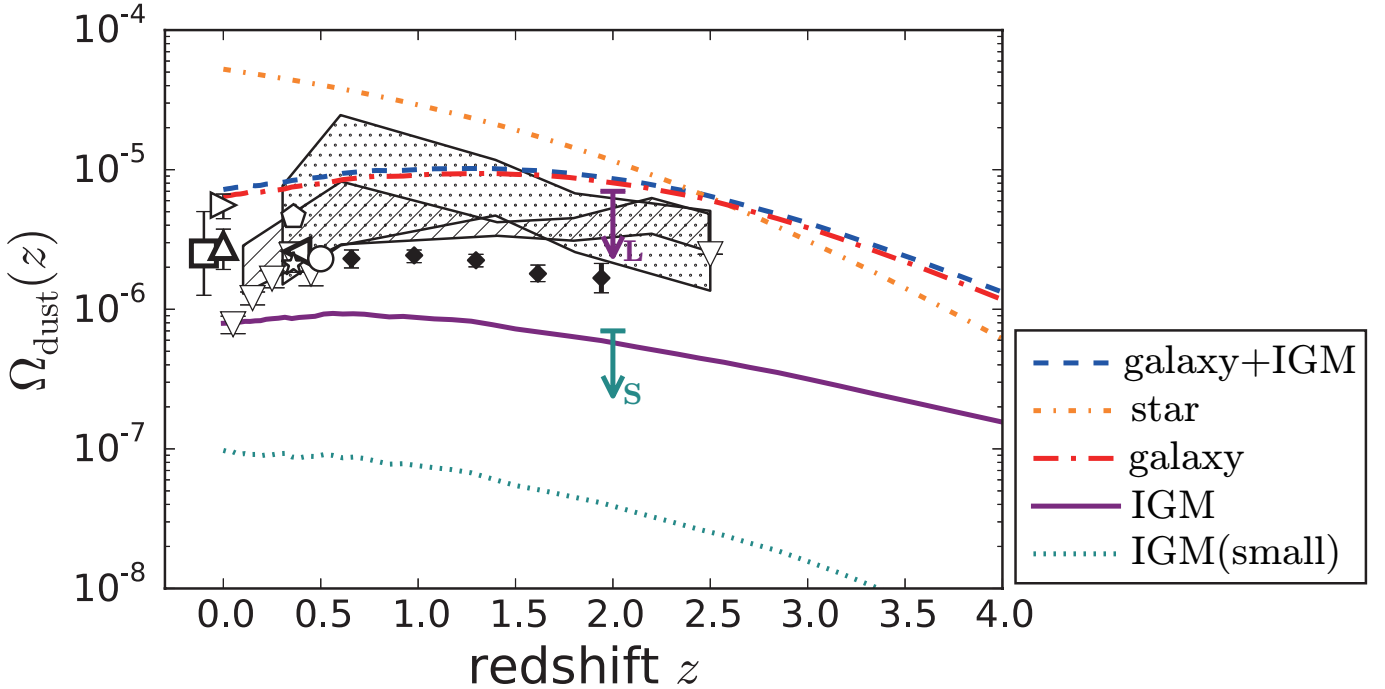


Figure 4. Redshift evolution of cosmic dust abundance $\Omega_{\text{dust}}(z)$ for various components. The blue dashed line labelled ‘galaxy+IGM’ shows the total amount of dust on gas particles inside simulated galaxies and the IGM. The red dot-long-dashed line labelled ‘galaxy’ presents only the amount of dust on gas particles inside simulated galaxies (the ISM and a part of the CGM). The purple solid line labelled ‘IGM’ is the amount of dust in the IGM. For the IGM component, we also show the small grain abundance with the mosgreen dotted line. The orange dot-short-dashed line labelled ‘star’ shows the total amount of dust absorbed into stars. We compare our results against the following observational results: the halo component of dust grains at $0.6 \lesssim z \lesssim 2$ (\blacklozenge) and $z = 0.5$ (\circ) from [Ménard & Fukugita \(2012\)](#). The open star is from [Ménard et al. \(2010\)](#). For the total abundance of dust grains in the Universe, \triangle , \triangleright , ∇ , \triangleleft , \square and pentagon are from [Driver et al. \(2007\)](#), [Clemens et al. \(2013\)](#), [Dunne et al. \(2011\)](#), [Fukugita \(2011\)](#), [Fukugita & Peebles \(2004\)](#) and [Ménard et al. \(2010\)](#), respectively. The hatched region and the dot-filled region are from [De Bernardis & Cooray \(2012\)](#) and [Thacker et al. \(2013\)](#), respectively. Upper limits of large and small grain abundance in the IGM from [Inoue & Kamaya \(2003\)](#) are shown with the purple (‘L’) and mosgreen (‘S’) arrows, respectively.

uously increases. As galaxies grow through their star formation activity (Fig. 1b), they are also enriched with metals and dust. The increase of metallicity further drives the dust enrichment through dust growth by accretion in the dense gas. The cosmic dust abundance continues to increase down to $z \sim 2$ (Fig. 4). Since accretion dominates the abundance of small grains in the metal-rich environment, the small grain abundance continue to increase even at $z < 2$ (Fig. 4). In our simulation, the comoving dust density peaks at $z = 1\text{--}2$, which coincides with the most dust enshrouded epoch in the Universe derived from *Herschel* observations ([Burgarella et al. 2013](#); [Driver et al. 2018](#)).

The cosmic dust density declines slightly at $z \lesssim 1$ because of astration. To support this, we also show the comoving dust density removed by astration in Fig. 4. At $z \sim 2$, more than half of dust grains are consumed by stars (astration). Interestingly, more than 80 per cent of the dust grains have been absorbed into stars by $z = 0$.

We also show the dust mass evolution in the IGM in Fig. 4. Both metals and dust are produced and spread into the IGM as a result of stellar production and feedback. The IGM is enriched with dust continuously; throughout all redshifts, almost all dust grains remain in the host galaxies, but about 10 per cent of the dust is ejected out of galaxies into the IGM.

In Fig. 4, we also present the observational data for the total dust abundance in various environments, which are obtained from integration of galactic dust emission and from fluctuation analysis of the cosmic infrared background radiation (CIRB). The total dust abundance in the simulated galaxies broadly agrees with the observed data from CIRB ([Thacker et al. 2013](#); [De Bernardis & Cooray 2012](#)) and the dust abundance in disk galaxies ([Driver et al. 2007](#)). However, we tend to overestimate the galactic dust amount compared with the observational estimates. This is because our identification of simulated galaxies includes their circumgalactic regions. As we show below in Section 3.4, a significant fraction of dust is contained in the CGM in our simulation. Observationally, [Ménard et al. \(2010\)](#) and [Peek et al. \(2015\)](#) found, based on the analysis of reddening of background QSOs, that the sum of the dust mass contained in the CGM is comparable to that existing in the galactic discs. The dust abundance estimated from Mg II absorbers ([Ménard & Fukugita 2012](#)) also indicates that a significant amount of dust is contained in the CGM. They argue that Mg II absorbers trace the CGM environment based on their impact parameters.

[Inoue & Kamaya \(2003\)](#) constrained the dust abundance in the IGM based on the observed thermal history

of the IGM.³ They argued that, if photoelectric heating by dust is significant, it heats the IGM too much to be consistent with its observed thermal history. By calculating the gas heating rate by dust grains and comparing it with the observed IGM temperatures at $2 \lesssim z \lesssim 4$ (Schaye et al. 2000), they obtained upper limits of $\Omega_{\text{dust}}^{\text{L}} < 7 \times 10^{-6}$ and $\Omega_{\text{dust}}^{\text{S}} < 7 \times 10^{-7}$ at $z \gtrsim 2$. Our simulation results are consistent with these upper limits.

A possible source of uncertainty in our galaxy/IGM dust abundance is the finite spatial resolution. We only identify the structures with $M_* > 10^8 M_{\odot}$ as galaxies (Section 2.5). In other words, small ‘galaxies’ whose stellar masses are less than $10^8 M_{\odot}$ are regarded not as a galaxy but as a part of the IGM. On the other hand, observations also have a similar problem because of their finite sensitivity and spatial resolution. Although it is extremely difficult to correct for the limited computational and observational capabilities, the above rough match between theory and observations indicates that the dust abundance in the cosmic volume can be broadly understood by the processes we included in the simulation (mainly stellar dust production and dust growth by accretion).

In Fig. 5, we show the time evolution of small and large grains for galaxies and the IGM. To clarify the relative abundance, we also show the small-to-large grain abundance ratio, $\Omega_{\text{dust}}^{\text{S}}/\Omega_{\text{dust}}^{\text{L}}$. The dust abundance in the Universe is always dominated by large grains. In galaxies, the redshift dependence of the small-to-large grain abundance ratio is flat. The large grain formation is dominated by stellar dust production and coagulation while the small grain formation is governed by shattering and accretion. If we sum up all galaxies, the statistics is dominated by small galaxies in which the major part of the dust is produced by stellar sources. The abundance of small grain is significant only in massive ($M_* \gtrsim 10^{10} M_{\odot}$) galaxies where shattering and accretion are efficient because of their high metallicity (Hou et al., in preparation).

In contrast, the small-to-large grain abundance ratio in the IGM monotonically increases from high redshift down to $z \sim 0$. The dust abundance in the IGM is fully dominated by large grains at high redshift because dust grains are ejected into the IGM before being processed by shattering and accretion, as discussed in Hou et al. (2017). The increase of the small-to-large grain abundance ratio in the IGM is due to the supply of small grains formed by shattering and accretion. Massive galaxies are assembled at low redshift ($z \lesssim 2$), and the ISM in massive galaxies contains a large amount of small grains. As a consequence, more small grains are supplied at lower redshift. *In situ* small-grain formation in the IGM by shattering may also be possible. However, we find that this path of small-grain formation is negligible because the grain–grain collision time-scale is longer than the cosmic age in the IGM. Indeed, we do not see any enhancement of the small grain abundance relative to the large grain abundance in the CGM as we see in Section 3.4 (Fig. 7). As shown later in this section, sputtering decreases both small and large grain abundances almost equally. Thus, the pro-

cessing in the IGM is not important in determining the grain size distribution in the IGM.

There is no observational data to compare for the grain size distribution in the IGM, while there are some observational clues in the CGM. Thus, the dust properties in the CGM may provide some insight into the IGM dust. As mentioned above, the dust properties in the CGM could be traced by Mg II absorbers as argued by Ménard & Fukugita (2012), who analyzed the background quasar (QSO: quasi-stellar object) data taken by the Sloan Digital Sky Survey (SDSS; York et al. 2000) in combination with *Galaxy Evolution Explorer* (GALEX; Martin et al. 2005) data. The reddening curves of Mg II absorbers are fitted well with the Small Magellanic Cloud (SMC) extinction curve, which indicates that dust grains smaller than $0.03 \mu\text{m}$ are abundant (Pei 1992; Weingartner & Draine 2001). However, our result shows that large grains dominate the IGM dust abundance (Fig. 4). Thus, there is a tension between our simulation results and the observed reddening curves for Mg II absorbers. We discuss this further in Sections 3.4 and 3.5.

We show the significance of sputtering in the hot gas (not associated with SNe) on the time evolution of the cosmic dust abundance in Fig. 5. As explained in Section 2.3, we select the hot gas not associated with SNe (mainly associated with the CGM and IGM) with the criterion $n_{\text{gas}} < 0.01 \text{ cm}^{-3}$ and $T_{\text{gas}} > 10^6 \text{ K}$. In Fig. 5, we indeed confirm that sputtering in the diffuse hot gas affects little the dust abundance in galaxies. In the IGM, in contrast, 70–80 per cent of the IGM dust could be destroyed by sputtering. Although small grains are more sensitive to sputtering than large grains, the ratio $\Omega_{\text{dust}}^{\text{S}}/\Omega_{\text{dust}}^{\text{L}}$ is not significantly affected by sputtering, as we observe in Fig. 5c. This is because the sputtering time-scales for both large and small grains are much shorter than the hydrodynamical time-scale, and almost all dust grains which suffer from sputtering are destroyed on the spot regardless of the grain size.

3.3 Dust mass function

The dust abundance in galaxies can also be expressed in the form of the dust mass function, which is the distribution function of dust mass in galaxies, as shown in Fig. 6. We compare the dust mass function of the simulated galaxies with observed dust mass functions. We have to keep in mind that observational estimates of dust mass depend on the adopted dust mass absorption coefficient (dust emissivity per dust mass). The observationally derived dust mass is simply proportional to κ_{850}^{-1} (κ_{850} is the dust mass absorption coefficient at a wavelength of $850 \mu\text{m}$), while the dust mass in our simulation is not affected by κ_{850} . We adopt a uniform dust mass absorption coefficient $\kappa_{850} = 0.77 \text{ cm}^2 \text{ g}^{-1}$ at $850 \mu\text{m}$ with a wavelength dependence of $\propto \lambda^{-2}$ according to Dunne et al. (2000). This value of κ_{850} is based on Dunne et al. (2000), and is intermediate between the values for graphite and silicates as given by Draine & Lee (1984) and Hughes et al. (1993). Draine (2003) claimed $\kappa_{850} = 0.383 \text{ cm}^2 \text{ g}^{-1}$, which is approximately a half of the above value. Thus, it is important to note that there is a factor 2–3 uncertainty in the dust mass derived from the observed IR emission.

Our simulation produces a larger number of galaxies

³ They define the radii of large grains as $10^{-2} \mu\text{m} \leq a \leq 10^{-1} \mu\text{m}$ and those of small grains as $a \sim 10^{-3} \mu\text{m}$.

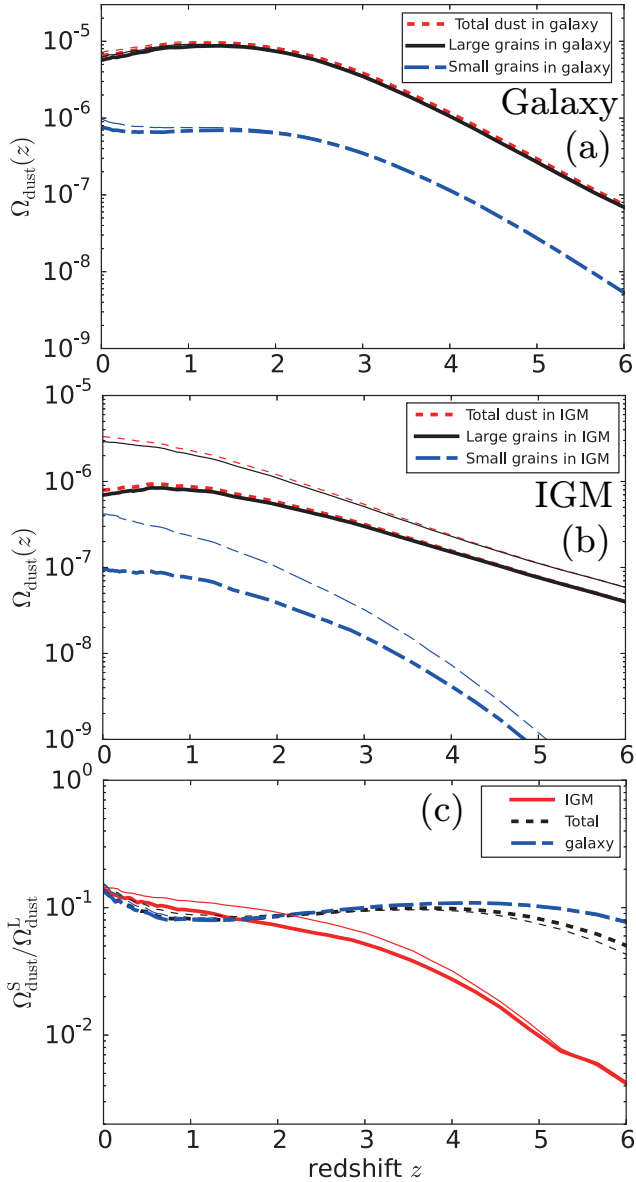


Figure 5. Panels (a) and (b): time evolution of cosmic dust abundance of large (thick solid line) and small grains (thick long-dashed-short-dashed line) in galaxies and in the IGM, respectively. The sum of large and small grains (‘Total’) is shown by the red thick dashed line in each panel. Panel (c): small-to-large grain abundance ratio for galaxies (blue long-dashed-short-dashed line), the IGM (red solid line), and the total (black dotted line). Thin lines in each panel represent the time evolution of each component without sputtering (i.e. $\tau_{sp}(a) \rightarrow +\infty$).

with high dust mass ($M_d \gtrsim 10^8 M_\odot$) at $z = 0$ than at $z = 2.4$, while the observational data indicate the opposite. As a result, although we reproduce the dust mass function at $z = 2.4$ well (if we consider a factor 2–3 uncertainty in the observational dust mass estimates), we overpredict the number of high- M_d galaxies at $z = 0$. Recalling that our simulation also overproduces the massive end in the galaxy stellar mass function (Fig. 1b), we argue that the overproduction of dusty galaxies is linked to that of massive galaxies. As discussed above, a possible reason is that we did not include AGN feedback. We expect that AGN feedback suppresses

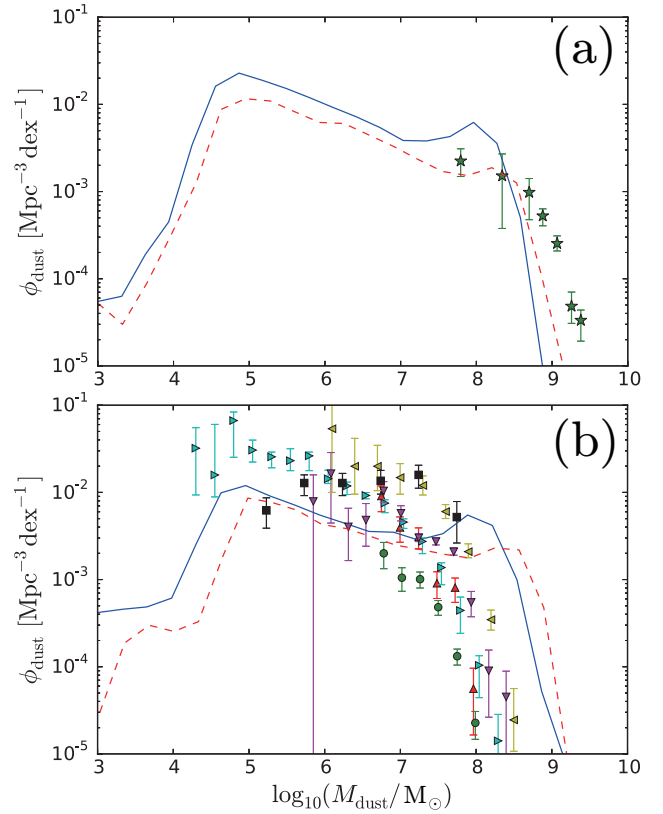


Figure 6. Dust mass function of simulated galaxies at $z = 2.4$ (panel (a)) and $z = 0$ (panel (b)) compared with observational results. The solid and dashed lines represent the result of L50N512 and L50N256, respectively. The symbols \star , \circ , ∇ , \triangleleft , \square and \triangle show the observational data taken from Dunne et al. (2003, 2000) Dunne et al. (2011); Clemens et al. (2013) Clark et al. (2015) and Vlahakis et al. (2005), respectively, while \triangleright is obtained from the IRAS PSCz-extrapolated mass function shown in Vlahakis et al. (2005).

the dust mass in two ways: (i) loss of dust by outflow, and/or (ii) suppression of star formation and subsequent chemical enrichment.

In Fig. 6, the cut-off at the low- M_d end ($\sim 10^4 M_\odot$) is determined by the spatial resolution of the simulation. Our simulation tends to underproduce the dust mass function at $M_d \sim 10^5$ – $10^7 M_\odot$, although it is marginally in the range of scatter of the observational data. The slope at $M_d \sim 10^5$ – $10^8 M_\odot$ is similar to the observed dust mass function. We should recall again that, on the observational side, there is a factor 2–3 uncertainty in the dust mass. Therefore we just conclude that our simulation qualitatively accounts for the observational dust mass function.

For comparison, we also show the dust mass function for the lower resolution run, L50N256. Although the mass resolution of L50N256 is eight times worse than that of L50N512, the amplitude and the cut-off of mass function at the massive end roughly agree with each other. This means that the mass resolution does not affect the statistical properties of dust mass in galaxies very much. As expected, the number of low-mass galaxies with $M_d \lesssim 10^5 M_\odot$ is higher for L50N512 than for L50N256 because of the higher mass resolution.

3.4 Circum-galactic dust around massive galaxies

Ménard et al. (2010) detected a large abundance of dust in the CGM by analyzing the correlation between the reddening of background QSOs and a large number of galaxies in the SDSS sample whose median redshift is $z \sim 0.3$. Peek et al. (2015) found a similar radial profile of CGM dust at $z \sim 0.05$. These studies showed that the dust mass in galaxy halos is comparable to that in galactic discs. In order to examine if our simulation also reproduces such a large dust abundance in galaxy halos (or in the CGM), we compare the radial profile of the surface density of dust up to ~ 1 Mpc from the galaxy centre.

We select 1617 simulated galaxies in the similar stellar mass range as the sample of Ménard et al. (2010)⁴, and computed the average radial profile of dust surface densities in the following way. We first extract the $(2\text{Mpc})^3$ region around each simulated galaxy at $z = 0$, and divide each region into a 200^3 cubic grid. Thus, the effective resolution of the radial profile is ~ 10 kpc. By calculating the averaged dust mass density at each grid point for small and large grains, we obtain the distribution of dust grains around the galaxies. Then, the 3-dimensional dust distribution is projected onto a 2-dimensional surface to obtain the radial profile of surface density as plotted in Fig. 7 (the projected radius is denoted as r).

In Fig. 7a, we compare our simulation result with the observations. We find that our total dust mass (the sum of small and large grains) can account for the observed dust abundance at $r \gtrsim 30$ kpc. We find that large grains dominate the total dust abundance in the entire circum-galactic region. The small-to-large grain mass ratio is $\sim 1/16$ at $r = 10$ kpc and $\sim 1/10$ at $r = 1$ Mpc. The dominance of large grains is also observed in the IGM as discussed in Section 3.2. The slightly lower small-to-large grain abundance ratio at the small radius is due to the continuous supply of large grains by coagulation.

We also plot the dust-to-metal surface density ratio, $\Sigma_{\text{dust}}/\Sigma_{\text{metal}}$, in Fig. 7b. The ratio is high (≈ 0.6) in the central region ($r < 20$ kpc), while it dramatically drops to ~ 0.25 at $r \approx 20$ kpc, and slowly decreases at $r > 20$ kpc because dust grains are destroyed by sputtering in hot ($T_{\text{gas}} > 10^6$ K) gas. At $r \gtrsim 200$ kpc, it drops to $\Sigma_{\text{dust}}/\Sigma_{\text{metal}} \approx 0.14$. A part of the dust still survives because not all the gas in the CGM is hot.

We compare the value of $\Sigma_{\text{dust}}/\Sigma_{\text{metal}}$ obtained in our simulation with that derived by Zu et al. (2011). They only calculated the spatial distribution of metals in the IGM and assumed a fixed dust-to-metal ratio (i.e. they did not calculate dust evolution) to obtain the dust distribution. They showed that $\Sigma_{\text{dust}}/\Sigma_{\text{metal}} \approx 0.24$ explains the dust abundance at $r \sim 1h^{-1}$ Mpc obtained by Ménard et al. (2010). They only normalized the amplitude of extinction at $1h^{-1}$ Mpc, but their prediction agreed with the result of Ménard et al. (2010) in a wide radius range of $0.01h^{-1}\text{Mpc} \lesssim r \lesssim$

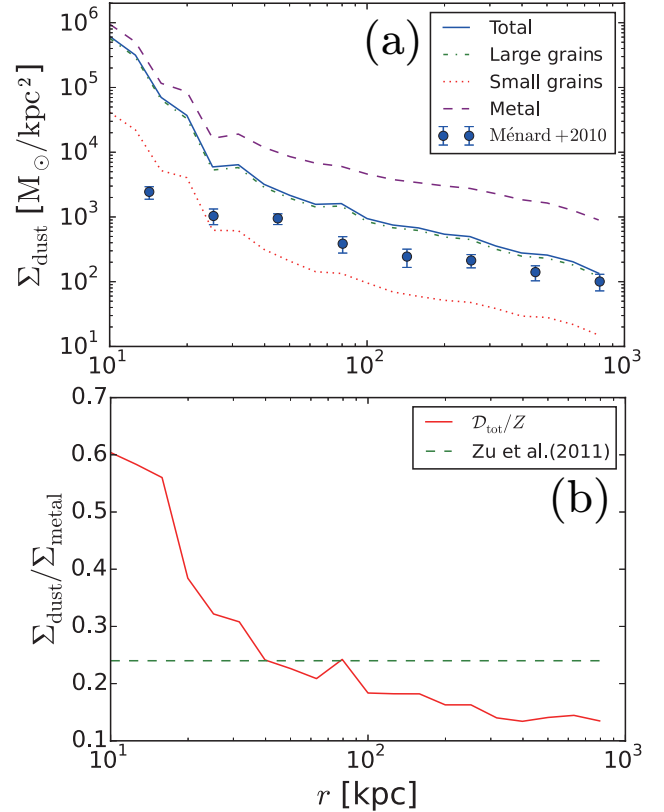


Figure 7. Panel (a): Averaged surface density profile of metals and dust around massive galaxies (r is the distance from the galaxy centre). We sampled all galaxies whose stellar mass is in the range of $10^{10}M_{\odot} \leq M_{*} \leq 10^{11}M_{\odot}$. The number of galaxies is 1617. The surface densities of metals and dust are presented with the dashed (purple) and solid (blue) lines, respectively. The blue and red dotted lines show the surface densities of large and small grains, respectively. Points with error bars are the observed radial profile of dust (Ménard et al. 2010). Panel (b): Radial profile of dust-to-metal surface density ratio. The dashed line shows the constant dust-to-metal ratio adopted by Zu et al. (2011).

$8h^{-1}\text{Mpc}$. Interestingly, our model that incorporated dust evolution in the simulation also predicts $\Sigma_{\text{dust}}/\Sigma_{\text{metal}} \sim 0.25$ at $0.02h^{-1}\text{Mpc} \lesssim r \lesssim 0.15h^{-1}\text{Mpc}$ without any tuning of dust-to-metal ratio.

3.5 Extinction of circum-galactic and intergalactic dust

The extinction over a cosmic distance (hereafter, referred to as the cosmic extinction) also puts a constraint on the dust properties in the cosmic volume. We calculate the cosmic extinction up to redshift z , $A_{\lambda}(z)$, in units of magnitude as (Ménard et al. 2010; Hirashita & Lin 2018)

$$\begin{aligned}
 A_{\lambda}(z) &= 2.5(\log_{10} e) \\
 &\times \int_0^z \left(\kappa^S(\lambda') \rho_{\text{dust}}^S(z') + \kappa^L(\lambda') \rho_{\text{dust}}^L(z') \right) \frac{c(1+z')^2}{H(z')} dz', \\
 \lambda &= \lambda' (1+z'), \\
 H(z) &= H_0 \sqrt{\Omega_m(1+z)^3 + \Omega_{\Lambda}}, \quad (14)
 \end{aligned}$$

⁴ Ménard et al. (2010) sampled galaxies with luminosity $L \approx 0.45L^*$ at $z = 0.3$, where L^* is the characteristic luminosity of the luminosity function at that redshift. Tomczak et al. (2014) reported the characteristic mass of the stellar mass function to be $\approx 10^{11.05}M_{\odot}$. If we assume $L \propto M_*$, a galaxy with $0.45L^*$ would have $M_* \approx 5 \times 10^{10}M_{\odot}$. Thus, we assume that Ménard et al. (2010)'s sample has a stellar mass range of $10^{10} < M_*/M_{\odot} < 10^{11}$.

where $\kappa^S(\lambda)$ and $\kappa^L(\lambda)$ are the dust mass extinction coefficient for small and large grains, respectively, as a function of wavelength, $\rho_{\text{dust}}^S(z)$ and $\rho_{\text{dust}}^L(z)$ are the comoving mass density of small and large grains as a function of redshift, respectively, c is the light speed, and $H(z)$ is the Hubble parameter at z . For the expression of $H(z)$, we assumed a flat Universe. We adopt the mass extinction coefficients from [Hou et al. \(2017\)](#), who assumed spherical and homogeneous dust grains with a mixture of silicate and graphite ([Draine & Lee 1984](#)) and applied the Mie theory ([Bohren & Huffman 1983](#)) based on the same optical constants in [Weingartner & Draine \(2001\)](#). In this paper, the mass fractions of silicate and carbonaceous dust are assumed to be 0.54 and 0.46, respectively ([Hirashita & Yan 2009](#)). Although these mass fractions give a good start (since we do not have any knowledge on the grain composition in the IGM), they should vary depending on the evolutionary stage of galaxy (e.g. [Pipino et al. 2011](#); [Bekki et al. 2015](#)). The production rate of each element also changes as a function of galaxy age (e.g. [Calura et al. 2014](#)). However, our conclusions regarding the cosmic extinction are not affected by the detailed mixture of the two dust species within the uncertainties in the observational constraint. An important conclusion drawn later about a flat extinction curve shape also holds regardless of the mixture ratio. We consider the cosmic extinction at $z > 0.3$, where some observational constraints are available. Because the comoving distance at $z = 0.3$ is 1.23 Gpc, which is much larger than the comoving scale of the large scale structure $\sim 100h^{-1}$ Mpc (e.g. [Eisenstein et al. 2005](#)), we are able to justify the usage of the mean density without considering the spatial inhomogeneity. Moreover, the observational constraints we adopt are derived from the analysis of a large number of objects in a large cosmic volume; thus, only averaged quantities are relevant for the analysis in this subsection.

We adopt the V-band wavelength ($0.55 \mu\text{m}$) at the observer's frame for λ , and show $A_V(z)$ in Fig. 8. For the dust mass densities, ρ_{dust}^S and ρ_{dust}^L , we examine two cases: in the first case, we adopt all the dust in the simulation box, while in the second case, we count only the dust in the IGM. The latter case is motivated by the fact that the observations of background QSOs used to derive the cosmic extinction are biased against lines of sight passing through galaxies where the extinction is high. That is, lines of sight without galaxies are preferentially sampled in the measurement of the cosmic extinction ([Vladilo & Péroux 2005](#)). Thus, we expect that observational results should lie between those two cases.

Cosmic dust extinction has been investigated in various ways. [More et al. \(2009\)](#) (marked by '1' in Fig. 8) focused on the effect of dust extinction on the apparent relation between the luminosity distance and the angular diameter distance of distant galaxies and obtained an upper limit on the cosmic dust extinction at $z \sim 0.35$. [Avgoustidis et al. \(2009\)](#) (marked by '2' in Fig. 8) put an upper limit on dust extinction by using the fact that dust grains decrease the apparent luminosity of SNe Ia and could affect the cosmological parameter estimates. [Mörtsell & Goobar \(2003\)](#) (marked by '3' in Fig. 8) made an attempt of finding systematic reddening for the SDSS QSO sample. They did not find such a systematic reddening and they set an upper limit of $A_V < 0.20$ at $z = 1$. [Ménard et al. \(2008\)](#) (marked by '4' in Fig. 8) observed the reddening of a statistical sample of Mg II ab-

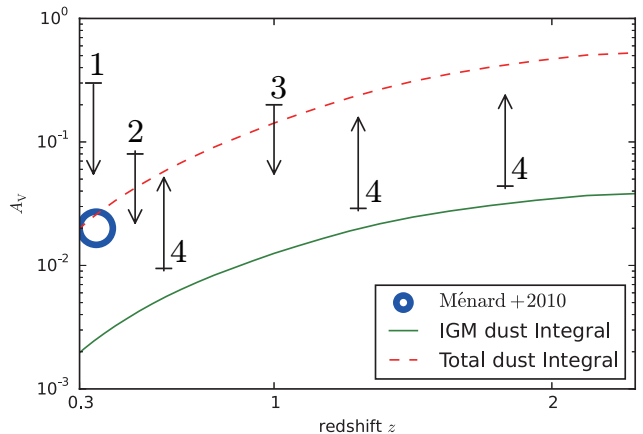


Figure 8. Cosmic dust extinction in the V band. The solid (green) and dashed (red) lines show the extinction by the IGM component and all dust grains in the simulation box, respectively. The numbers '1', '2', '3' and '4' are observational constraints obtained by [More et al. \(2009\)](#), [Avgoustidis et al. \(2009\)](#), [Mörtsell & Goobar \(2003\)](#) and [Ménard et al. \(2008\)](#). The circle indicates the estimate based on the statistics of halo extinction by [Ménard et al. \(2010\)](#).

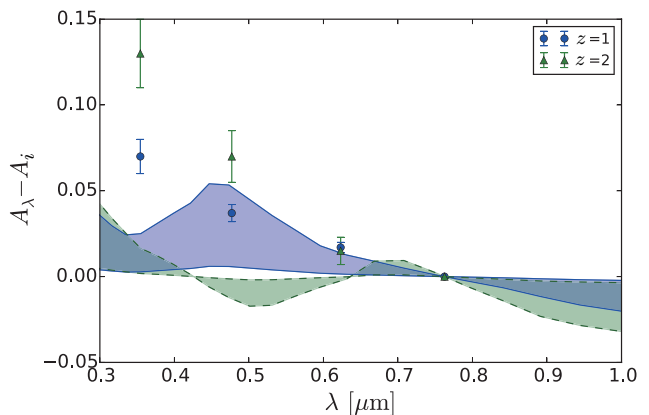


Figure 9. Estimated reddening curves of Mg II absorbers. The solid (blue) and dashed (green) lines represent the curves at $z = 1$ and 2 , respectively. The shaded area associated with these lines show the range of the column densities assumed in the calculation. The filled circles and triangles with error bars are observational data taken from [Ménard & Fukugita \(2012\)](#).

sorbers. Since they only counted Mg II absorbers, the estimated extinction is regarded as a lower limit. [Ménard et al. \(2010\)](#) estimated the cosmic extinction at $z \sim 0.3$ on the assumption that it is dominated by dust in galaxy halos.

As mentioned above, we expect that the actually observed cosmic extinction would lie between the cosmic extinction arising from all the dust in the cosmic volume and that contributed from only the IGM dust (shown by the dashed and solid lines in Fig. 8, respectively). In Fig. 8, we indeed find that the observational constraints are broadly located between those two lines. This indicates that our dust abundance in the cosmic volume agrees with the observational constraints on the cosmic extinction.

The wavelength dependence of extinction could provide useful information on the grain size (e.g. [Mathis et al. 1977](#)). Therefore, we further calculate the extinction (or reddening)

curve, which could be compared with observations. Following Ménard & Fukugita (2012), we assume that Mg II absorbers trace the medium in galaxy halos. Peek et al. (2015) have shown that the reddening curves in galaxy halos are indeed similar to those in Mg II absorbers. Because the column density is important for the reddening, using Mg II absorbers is advantageous because of their known column densities.

The extinction at wavelength λ is estimated by the following formula (Hirashita & Lin 2018):

$$A_\lambda = 2.5(\log_{10} e)\mu m_{\text{H}} N_{\text{H}}^{\text{MgII}} \left(\kappa^{\text{L}}(\lambda) \mathcal{D}_{\text{L}}^{\text{MgII}} + \kappa^{\text{S}}(\lambda) \mathcal{D}_{\text{S}}^{\text{MgII}} \right), \quad (15)$$

where μ is the gas mass per hydrogen ($\mu = 1.4$), m_{H} is the mass of hydrogen atom, $N_{\text{H}}^{\text{MgII}}$ is the hydrogen column density of an Mg II absorber, and $\mathcal{D}_{\text{L}}^{\text{MgII}}$ and $\mathcal{D}_{\text{S}}^{\text{MgII}}$ are the large and small grain abundances (dust-to-gas ratios) in Mg II absorbers. We adopt $N_{\text{H}} = 10^{19.5} \text{ cm}^{-2}$, which is derived as a geometric mean for an Mg II absorber sample by Ménard & Chelouche (2009). According to Ménard & Chelouche (2009), the dust-to-gas ratio is 60–80 per cent of the Milky Way value if we use $A_{\text{V}}/N_{\text{H}}^{\text{MgII}}$ for the indicator of dust-to-gas ratio. Assuming the typical dust-to-gas ratio of the Milky Way to be 0.01 (or slightly less) (e.g. Pei 1992), we adopt the total dust-to-gas ratio for Mg II absorbers as $\mathcal{D}_{\text{tot}}^{\text{MgII}} = 0.006$. We assume that the small-to-large grain abundance ratio in Mg II absorbers is equal to that in the IGM:

$$\mathcal{D}_{\text{L}}^{\text{MgII}} = \frac{\Omega_{\text{dust,IGM}}^{\text{L}}}{\Omega_{\text{dust,IGM}}^{\text{S}}} \mathcal{D}_{\text{tot}}^{\text{MgII}}, \quad (16)$$

$$\mathcal{D}_{\text{S}}^{\text{MgII}} = \frac{\Omega_{\text{dust,IGM}}^{\text{S}}}{\Omega_{\text{dust,IGM}}^{\text{L}}} \mathcal{D}_{\text{tot}}^{\text{MgII}}. \quad (17)$$

where $\Omega_{\text{IGM dust}}^{\text{L}}$, $\Omega_{\text{IGM dust}}^{\text{S}}$ and $\Omega_{\text{IGM dust}}$ are introduced in Section 3.2. Considering the uncertainties in the column density and the dust-to-gas ratio, we examine an order-of-magnitude range of $N_{\text{H}}^{\text{MgII}} = 10^{19} - 10^{20} \text{ cm}^{-2}$ (while we fix $\mathcal{D}_{\text{tot}}^{\text{MgII}} = 0.006$ because of the degeneracy between N_{H} and $\mathcal{D}_{\text{tot}}^{\text{MgII}}$).

For the reddening, we plot the difference from the extinction in the i -band, $A_\lambda - A_i$ (note that only such a ‘reddening’ is measurable in the observation) in Fig. 9. Here, we show the wavelength in the observer’s frame [thus, apply $\lambda/(1+z)$ for λ in equation (15)]. The wavelength dependence of reddening is referred to as the reddening curve. We plot the reddening curves of Mg II absorbers at $z = 1$ and 2 in Fig. 8. Our model predicts reddening curves marginally consistent with the observational data at $z = 1$ except at the shortest wavelength. There is a clear discrepancy between the reddening curve in our simulation and the observational data at $z = 2$. The reason why the estimated extinction curve is very flat is that the dust abundance in the IGM is dominated by large grains in our simulation as shown in Section 3.2. Therefore, there is a tension between the simulation and the observation in terms of the grain size distribution at $z = 2$. On the other hand, the abundance of small grains at $z = 1$ becomes greater than that at $z = 2$; accordingly, the estimated extinction curve at $z = 1$ becomes relatively steep and able to explain a couple of observational points. We further discuss the discrepancy between our results and the observation data in Section 4.2.

4 DISCUSSION

4.1 Comparison with other theoretical studies on CGM/IGM dust

The spatial distribution of dust in the CGM and IGM has been predicted by cosmological hydrodynamical simulations (e.g. McKinnon et al. 2016, 2017) and semi-analytic models (e.g. Popping et al. 2017). The radial profile of dust surface density in McKinnon et al. (2017) is steeper than the observational data by Ménard et al. (2010) in the range $r < 100$ kpc and flatter at $r > 100$ kpc. McKinnon et al. (2017) underproduced the dust abundances relative to those reported by Ménard et al. (2010). We predict a mild slope for the radial profile compared to that in McKinnon et al. (2017) except in the central region. As a consequence, our result widely agrees with the observed profile by Ménard et al. (2010). Popping et al. (2017) estimated the dust abundance in hot halos as a function of halo mass, and predicted a comparable halo dust mass to that observed in Peek et al. (2015) for galaxies with $M_* \sim 10^{10} M_\odot$.

The spatial dust distribution in the CGM and IGM highly depends on the feedback model. The distribution of dust grains around massive galaxies was also simulated by Zu et al. (2011) based on their metallicity distribution under a fixed dust-to-metal ratio. They adopted a momentum-driven wind model, which was claimed originally by Martin (2005) and Murray et al. (2005) as a physically reasonable feedback model. Zu et al. (2011) tuned the dust-to-metal ratio and varied the feedback strength. In our work, we roughly reproduced the observed radial profile without fixing the dust-to-metal ratio: in the central region ($r \lesssim 20$ kpc), dust growth by accretion is active and the dust-to-metal ratio is high (≈ 0.6), whereas it drops to ~ 0.3 at $r \sim 20$ kpc and gradually decreases to ~ 0.14 at $r \sim 1$ Mpc. This decrease is due to the dust destruction in the hot gas. Therefore, our model suggests that there is a significant variation in the dust-to-metal ratio of the CGM/IGM. Importantly, there is a systematic decrease in the dust-to-metal ratio along the distance from the galaxy centre. It would be interesting to reexamine Zu et al. (2011)’s analysis by taking the variation in the dust-to-metal ratio into account.

4.2 Issues for circum-galactic and intergalactic extinctions

As mentioned in Section 3.4, small grains are deficient in the IGM and CGM in our simulation. This leads to a flat reddening curve, which does not fit to the actually observed curve for Mg II absorbers. A possible reason for this discrepancy is that our simulation failed to fully include the physical processes important for dust in the CGM and IGM. For example, we did not include radiation pressure that could be important in transporting dust out of the galaxies (Ferrara et al. 1991; Bianchi & Ferrara 2005). However, there is no physical reason that radiation pressure preferentially transport small grains; thus, radiation pressure will not make the reddening curve in the IGM and CGM steeper. Another possibility is that our simulation failed to treat the hydrodynamical effects (especially, shocks and turbulence) in galaxy outflows because of low spatial resolution. Some authors argue that Mg II absorbers originate

from outflows driven by active star formation (Norman et al. 1996; Bond et al. 2001). In such a high-velocity environment, shocks or high-velocity turbulence could be induced. Both shocks (Jones et al. 1996) and turbulence (Yan et al. 2004; Hirashita & Yan 2009) can cause grain shattering. Since our simulation is not capable of resolving shocks and turbulence, this production path of small grain by shattering could not be successfully treated. It would be interesting to investigate the possibility of shattering in outflows using higher resolution zoom-in simulations.

The lack of small grains leads to a significantly flatter reddening curve than the observed one by Ménard & Fukugita (2012) as shown in Fig. 9. The assumption on the reddening or extinction curve is crucial in converting the observed reddening to the dust abundance. Ménard et al. (2010) and Ménard & Fukugita (2012) adopted the SMC extinction curve to derive the dust abundance in galaxy halos. A steeper extinction curve requires a smaller amount of dust to explain a certain amount of reddening. Therefore, if our calculation is correct and the extinction curve is flat, the CGM and IGM contain more dust than estimated by Ménard et al. (2010) and Ménard & Fukugita (2012). However, the observational analysis in Peek et al. (2015) shows that galaxy halos at $z \sim 0.05$ show a steep extinction curve similar to the SMC curve. Therefore, more efforts on the theoretical side would be required to investigate the possibilities of small grain production in the CGM and IGM.

4.3 Possible importance of AGN feedback

In order to concentrate on the issues related to stellar processes, we did not include AGN feedback in this paper. As we showed above, the stellar mass function and the dust mass function are both overestimated at the massive end (Figs. 1 and 6). Such an overestimate could be resolved by implementation of AGN feedback as done in various models (e.g. Harrison 2017; Sijacki et al. 2015; Weinberger et al. 2017; Fiacconi et al. 2018), some of which took radiative feedback from AGNs into account (e.g. Vogelsberger et al. 2014). The importance for gas heating is also reported observationally (e.g. Fabian 2012). We expect that AGN feedback suppresses the formation of dense clouds, where dust grains grow efficiently. This suppression of dust growth together with the effect of mass ejection will decrease the number of dust-rich galaxies. Vogelsberger et al. (2014) claimed that the gas heated by AGNs could enhance dust destruction by sputtering. This affects the dust abundance in the CGM and IGM. The above effects overall suppress the dust abundance, especially in or around massive galaxies.

However, the effects of AGN may not be so simple. Pipino et al. (2011) already developed a model that can treat the evolution of dust in QSOs. In their model, QSOs are regarded as progenitors of elliptical galaxies. Therefore, the development of AGNs could be tightly related to the host galaxy properties (see also Valiante et al. 2011). Hirashita & Nozawa (2017) suggest that the AGN feedback could create a cycle of gas cooling and heating, which would cause a cyclic behaviour of dust mass increase and decrease with a period of AGN feedback. Elvis et al. (2002) suggested positive feedback to the dust abundance by pointing out that dust could condense in AGN-driven winds. Therefore, clar-

ifying the effects of AGN feedback on the dust abundance requires inclusion of the above negative and positive influences and an appropriate modelling of the host galaxies.

5 CONCLUSION

We investigate the dust evolution using a cosmic hydrodynamical simulation by extending our previous single-galaxy simulations in A17 and Hou et al. (2017). The grain size distribution is also treated in the bimodal form of large and small grains, with a grain radius boundary of $\sim 0.03 \mu\text{m}$. In our simulation, we take into account not only dust generation by SNe and AGB stars but also dust growth by accretion. We also include other interstellar processing mechanisms such as dust destruction by SN shocks, coagulation in the dense ISM, and shattering in the diffuse ISM. For dust destruction, coagulation, and accretion, we adopt the sub-grid models developed in A17.

We first confirm that the relation between dust-to-gas ratio and metallicity for the simulated galaxies is consistent with the observed relation at $z = 0$. In particular the nonlinear increase of dust-to-gas ratio as a function of metallicity at $Z \gtrsim 0.1 Z_{\odot}$ is described well by the transition from the dust production dominated by stellar sources, to that dominated by accretion (dust growth). The consistency with the observational data suggests that the implementation of dust abundance evolution is successful in our simulation. After confirming this, we put particular focus on the cosmological-volume properties of dust without going into detailed analysis of individual galaxies, which will be reported in a separate paper (Hou et al., in preparation).

We present the comoving density of dust mass as a function of redshift. The comoving dust mass density in our simulation is roughly consistent with the one derived from the analysis of observed infrared radiation at $z < 2.4$. In our simulation, the peak of the comoving dust density lies at $z = 1-2$, which coincides with the most dust-enshrouded epoch in the Universe derived from *Herschel* observations (Burgarella et al. 2013). We also find that the dust abundance in the IGM is always dominated by large grains.

The statistical properties of dust in galaxies are also investigated using the dust mass function. Our simulation reproduces the dust mass function at $z = 2.4$ well. At $z = 0$, it broadly accounts for the observational slope of dust mass function at $M_d \sim 10^5-10^8 M_{\odot}$, but is in excess at the massive end. The excess could be improved if we include AGN feedback in the simulation.

We further investigate the dust properties in the IGM and CGM. For the CGM, we examine the radial profile of dust surface density around galaxies with $M_* = 10^{10}-10^{11} M_{\odot}$ up to $r = 1 \text{ Mpc}$, and find that we reproduce the observed radial profile at $r > 20 \text{ kpc}$. This means that our stellar feedback model is successfully transporting the dust formed in galaxies to the circum-galactic region. However, we also find that the dust abundance dominated by large grains is not consistent with the steep reddening curve derived for Mg II absorbers at $z = 1$ and 2 (Ménard & Fukugita 2012). This indicates that our simulation still fails to include a mechanism of supplying small grains to the CGM/IGM. We predict that the dust-to-metal ratio in the halo decreases with increasing r , since dust grains in the CGM/IGM are

destroyed by hot gas via sputtering. Using the dust properties in the simulation, we predict cosmological reddening of $A_V \sim 10^{-2}$ at $z = 0.3$ while $A_V \sim 10^{-1}$ at $z = 2.0$. Both values satisfy the observational constraints.

ACKNOWLEDGMENT

We thank the anonymous referee for careful reading and useful comments. We are grateful to Volker Springel for providing us with the original version of GADGET-3 code. Numerical computations were carried out on Cray XC30 at the Center for Computational Astrophysics, National Astronomical Observatory of Japan and XL at the Theoretical Institute for Advanced Research in Astrophysics (TIARA) in Academia Sinica. HH thanks the Ministry of Science and Technology for financial support through MOST 105-2112-M-001-027-MY3 and MOST 107-2923-M-001-003-MY3. This work was in part supported by JSPS KAKENHI Grant Number JP17H01111.

REFERENCES

- Aoyama S., Hou K.-C., Shimizu I., Hirashita H., Todoroki K., Choi J.-H., Nagamine K., 2017, *MNRAS*, **466**, 105
- Asano R. S., Takeuchi T. T., Hirashita H., Inoue A. K., 2013a, *Earth, Planets, and Space*, **65**, 213
- Asano R. S., Takeuchi T. T., Hirashita H., Nozawa T., 2013b, *MNRAS*, **432**, 637
- Asano R. S., Takeuchi T. T., Hirashita H., Nozawa T., 2014, *MNRAS*, **440**, 134
- Avgoustidis A., Verde L., Jimenez R., 2009, *J. Cosmology Astropart. Phys.*, **6**, 012
- Barlow M. J., Silk J., 1976, *ApJ*, **207**, 131
- Bekki K., 2013a, *MNRAS*, **432**, 2298
- Bekki K., 2013b, *MNRAS*, **436**, 2254
- Bekki K., 2015, *MNRAS*, **449**, 1625
- Bekki K., Hirashita H., Tsujimoto T., 2015, *ApJ*, **810**, 39
- Bianchi S., Ferrara A., 2005, *MNRAS*, **358**, 379
- Bohren C. F., Huffman D. R., 1983, Absorption and scattering of light by small particles. A Wiley-Interscience Publication
- Bohren C. F., Huffman D. R., Kam Z., 1983, *Nature*, **306**, 625
- Bond N. A., Churchill C. W., Charlton J. C., Vogt S. S., 2001, *ApJ*, **562**, 641
- Bouwens R. J., et al., 2009, *ApJ*, **705**, 936
- Buat V., Boselli A., Gavazzi G., Bonfanti C., 2002, *A&A*, **383**, 801
- Burgarella D., et al., 2013, *A&A*, **554**, A70
- Calura F., Pipino A., Matteucci F., 2008, *A&A*, **479**, 669
- Calura F., Gilli R., Vignali C., Pozzi F., Pipino A., Matteucci F., 2014, *MNRAS*, **438**, 2765
- Calzetti D., Armus L., Bohlin R. C., Kinney A. L., Koornneef J., Storchi-Bergmann T., 2000, *ApJ*, **533**, 682
- Cazaux S., Spaans M., 2009, *A&A*, **496**, 365
- Cazaux S., Tielens A. G. G. M., 2004, *ApJ*, **604**, 222
- Choi J.-H., Nagamine K., 2012, *MNRAS*, **419**, 1280
- Clark C. J. R., et al., 2015, *MNRAS*, **452**, 397
- Clemens M. S., et al., 2013, *MNRAS*, **433**, 695
- Dayal P., Hirashita H., Ferrara A., 2010, *MNRAS*, **403**, 620
- De Bernardis F., Cooray A., 2012, *ApJ*, **760**, 14
- Dobbs C. L., Pringle J. E., 2013, *MNRAS*, **432**, 653
- Draine B. T., 2003, *ARA&A*, **41**, 241
- Draine B. T., Lee H. M., 1984, *ApJ*, **285**, 89
- Draine B. T., Salpeter E. E., 1979, *ApJ*, **231**, 77
- Driver S. P., Popescu C. C., Tuffs R. J., Liske J., Graham A. W., Allen P. D., de Propriis R., 2007, *MNRAS*, **379**, 1022
- Driver S. P., et al., 2018, *MNRAS*, **475**, 2891
- Duffy A. R., Mutch S. J., Poole G. B., Geil P. M., Kim H.-S., Mesinger A., Wyithe J. S. B., 2017, *MNRAS*, **470**, 3300
- Dunne L., Eales S., Edmunds M., Ivison R., Alexander P., Clements D. L., 2000, *MNRAS*, **315**, 115
- Dunne L., Eales S. A., Edmunds M. G., 2003, *MNRAS*, **341**, 589
- Dunne L., et al., 2011, *MNRAS*, **417**, 1510
- Dwek E., 1998, *ApJ*, **501**, 643
- Eisenstein D. J., et al., 2005, *ApJ*, **633**, 560
- Elvis M., Marengo M., Karovska M., 2002, *ApJ*, **567**, L107
- Fabian A. C., 2012, *ARA&A*, **50**, 455
- Ferrara A., Ferrini F., Barsella B., Franco J., 1991, *ApJ*, **381**, 137
- Fiacconi D., Sijacki D., Pringle J. E., 2018, *MNRAS*, **477**, 3807
- Fukugita M., 2011, preprint, ([arXiv:1103.4191](https://arxiv.org/abs/1103.4191))
- Fukugita M., Peebles P. J. E., 2004, *ApJ*, **616**, 643
- Ginolfi M., Graziani L., Schneider R., Marassi S., Valiante R., Dell'Agli F., Ventura P., Hunt L. K., 2018, *MNRAS*, **473**, 4538
- Gioannini L., Matteucci F., Calura F., 2017, *MNRAS*, **471**, 4615
- Gjergo E., Granato G. L., Murante G., Ragone-Figueroa C., Tornatore L., Borgani S., 2018, preprint, ([arXiv:1804.06855](https://arxiv.org/abs/1804.06855))
- Gould R. J., Salpeter E. E., 1963, *ApJ*, **138**, 393
- Hahn O., Abel T., 2011, *MNRAS*, **415**, 2101
- Harrison C. M., 2017, *Nature Astronomy*, **1**, 0165
- Hirashita H., 2015, *MNRAS*, **447**, 2937
- Hirashita H., Ferrara A., 2002, *MNRAS*, **337**, 921
- Hirashita H., Kuo T.-M., 2011, *MNRAS*, **416**, 1340
- Hirashita H., Lin C.-Y., 2018, preprint, ([arXiv:1804.00848](https://arxiv.org/abs/1804.00848))
- Hirashita H., Nozawa T., 2017, *Planet. Space Sci.*, **149**, 45
- Hirashita H., Yan H., 2009, *MNRAS*, **394**, 1061
- Hirashita H., Nozawa T., Villaume A., Srinivasan S., 2015, *MNRAS*, **454**, 1620
- Hou K.-C., Hirashita H., Nagamine K., Aoyama S., Shimizu I., 2017, *MNRAS*, **469**, 870
- Hughes D. H., Robson E. I., Dunlop J. S., Gear W. K., 1993, *MNRAS*, **263**, 607
- Inoue A. K., 2011, *Earth, Planets, and Space*, **63**, 1027
- Inoue A. K., Kamaya H., 2003, *MNRAS*, **341**, L7
- Ishiki S., Okamoto T., 2017, *MNRAS*, **466**, L123
- Jaacks J., Nagamine K., Choi J. H., 2012, *MNRAS*, **427**, 403
- Jaacks J., Thompson R., Nagamine K., 2013, *ApJ*, **766**, 94
- Jones A. P., Tielens A. G. G. M., Hollenbach D. J., 1996, *ApJ*, **469**, 740
- Kennicutt R. C., Evans N. J., 2012, *ARA&A*, **50**, 531
- Kuo T.-M., Hirashita H., 2012, *MNRAS*, **424**, L34
- Larson R. B., 1981, *MNRAS*, **194**, 809
- Larson R. B., 2005, *MNRAS*, **359**, 211
- Lisenfeld U., Ferrara A., 1998, *ApJ*, **496**, 145
- Madau P., Pozzetti L., Dickinson M., 1998, *ApJ*, **498**, 106
- Martin C. L., 2005, *ApJ*, **621**, 227
- Martin D. C., et al., 2005, *ApJ*, **619**, L1
- Mathis J. S., Rumpl W., Nordsieck K. H., 1977, *ApJ*, **217**, 425
- Mattsson L., De Cia A., Andersen A. C., Zafar T., 2014, *MNRAS*, **440**, 1562
- McCarthy I. G., Schaye J., Bird S., Le Brun A. M. C., 2017, *MNRAS*, **465**, 2936
- McKinnon R., Torrey P., Vogelsberger M., 2016, *MNRAS*, **457**, 3775
- McKinnon R., Torrey P., Vogelsberger M., Hayward C. C., Marinacci F., 2017, *MNRAS*, **468**, 1505
- McKinnon R., Vogelsberger M., Torrey P., Marinacci F., Kannan R., 2018, *MNRAS*,
- Ménard B., Chelouche D., 2009, *MNRAS*, **393**, 808
- Ménard B., Fukugita M., 2012, *ApJ*, **754**, 116
- Ménard B., Nestor D., Turnshek D., Quider A., Richards G., Chelouche D., Rao S., 2008, *MNRAS*, **385**, 1053
- Ménard B., Scranton R., Fukugita M., Richards G., 2010, *MNRAS*, **405**, 1025
- More S., Bovy J., Hogg D. W., 2009, *ApJ*, **696**, 1727

Mörtsell E., Goobar A., 2003, *J. Cosmology Astropart. Phys.*, **9**, 009

Moustakas J., et al., 2013, *ApJ*, **767**, 50

Murray N., Quataert E., Thompson T. A., 2005, *ApJ*, **618**, 569

Nagamine K., Fukugita M., Cen R., Ostriker J. P., 2001, *ApJ*, **558**, 497

Nagamine K., Springel V., Hernquist L., Machacek M., 2004, *MNRAS*, **350**, 385

Nagamine K., Reddy N., Daddi E., Sargent M. T., 2016, *Space Sci. Rev.*, **202**, 79

Norman C. A., Bowen D. V., Heckman T., Blades C., Danly L., 1996, *ApJ*, **472**, 73

Nozawa T., Fukugita M., 2013, *ApJ*, **770**, 27

Nozawa T., Kozasa T., Habe A., 2006, *ApJ*, **648**, 435

Nozawa T., Asano R. S., Hirashita H., Takeuchi T. T., 2015, *MNRAS*, **447**, L16

Omukai K., 2000, *ApJ*, **534**, 809

Omukai K., Tsuribe T., Schneider R., Ferrara A., 2005, *ApJ*, **626**, 627

Peek J. E. G., Ménard B., Corrales L., 2015, *ApJ*, **813**, 7

Pei Y. C., 1992, *ApJ*, **395**, 130

Pillepich A., et al., 2018, *MNRAS*, **473**, 4077

Pipino A., Fan X. L., Matteucci F., Calura F., Silva L., Granato G., Maiolino R., 2011, *A&A*, **525**, A61

Planck Collaboration et al., 2016, *A&A*, **594**, A13

Popping G., Somerville R. S., Galametz M., 2017, *MNRAS*, **471**, 3152

Reddy N. A., Steidel C. C., 2009, *ApJ*, **692**, 778

Rémy-Ruyer A., et al., 2014, *A&A*, **563**, A31

Saitoh T. R., 2017, *AJ*, **153**, 85

Schaller M., Dalla Vecchia C., Schaye J., Bower R. G., Theuns T., Crain R. A., Furlong M., McCarthy I. G., 2015, *MNRAS*, **454**, 2277

Schaye J., Theuns T., Rauch M., Efstathiou G., Sargent W. L. W., 2000, *MNRAS*, **318**, 817

Schaye J., et al., 2015, *MNRAS*, **446**, 521

Schimminovich D., et al., 2005, *ApJ*, **619**, L47

Schneider R., Omukai K., Inoue A. K., Ferrara A., 2006, *MNRAS*, **369**, 1437

Shimizu I., Inoue A. K., Okamoto T., Yoshida N., 2014, *MNRAS*, **440**, 731

Shimizu I., Inoue A. K., Okamoto T., Yoshida N., 2016, *MNRAS*, **461**, 3563

Sijacki D., Vogelsberger M., Genel S., Springel V., Torrey P., Snyder G. F., Nelson D., Hernquist L., 2015, *MNRAS*, **452**, 575

Springel V., 2005, *MNRAS*, **364**, 1105

Springel V., Yoshida N., White S. D. M., 2001a, *New Astron.*, **6**, 79

Springel V., White S. D. M., Tormen G., Kauffmann G., 2001b, *MNRAS*, **328**, 726

Steidel C. C., Adelberger K. L., Giavalisco M., Dickinson M., Pettini M., 1999, *ApJ*, **519**, 1

Sutherland R. S., Dopita M. A., 1993, *ApJS*, **88**, 253

Takeuchi T. T., Buat V., Burgarella D., 2005, *A&A*, **440**, L17

Takeuchi T. T., Buat V., Heinis S., Giovannoli E., Yuan F.-T., Iglesias-Páramo J., Murata K. L., Burgarella D., 2010, *A&A*, **514**, A4

Takeuchi T. T., Yuan F.-T., Ikeyama A., Murata K. L., Inoue A. K., 2012, *ApJ*, **755**, 144

Thacker C., et al., 2013, *ApJ*, **768**, 58

Thompson R., Nagamine K., Jaacks J., Choi J.-H., 2014, *ApJ*, **780**, 145

Tomczak A. R., et al., 2014, *ApJ*, **783**, 85

Tsai J. C., Mathews W. G., 1995, *ApJ*, **448**, 84

Valiante R., Schneider R., Salvadori S., Bianchi S., 2011, *MNRAS*, **416**, 1916

Vladilo G., Péroux C., 2005, *A&A*, **444**, 461

Vlahakis C., Dunne L., Eales S., 2005, *MNRAS*, **364**, 1253

Vogelsberger M., Genel S., Sijacki D., Torrey P., Springel V., Hernquist L., 2013, *MNRAS*, **436**, 3031

Vogelsberger M., et al., 2014, *MNRAS*, **444**, 1518

Weinberger R., et al., 2017, *MNRAS*, **465**, 3291

Weingartner J. C., Draine B. T., 2001, *ApJ*, **548**, 296

Whitworth A. P., Boffin H. M. J., Francis N., 1998, *MNRAS*, **299**, 554

Yajima H., Shlosman I., Romano-Díaz E., Nagamine K., 2015, *MNRAS*, **451**, 418

Yamasawa D., Habe A., Kozasa T., Nozawa T., Hirashita H., Umeda H., Nomoto K., 2011, *ApJ*, **735**, 44

Yan H., Lazarian A., Draine B. T., 2004, *ApJ*, **616**, 895

York D. G., et al., 2000, *AJ*, **120**, 1579

Zhukovska S., Gail H.-P., Trieloff M., 2008, *A&A*, **479**, 453

Zhukovska S., Dobbs C., Jenkins E. B., Klessen R. S., 2016, *ApJ*, **831**, 147

Zu Y., Weinberg D. H., Davé R., Fardal M., Katz N., Kereš D., Oppenheimer B. D., 2011, *MNRAS*, **412**, 1059

APPENDIX A: EVOLUTION OF DUST ABUNDANCES

We show the derivation of equations (5) and (6). The time evolution of gas mass [$m_{g(i)}(t)$], large grain mass [$m_{L(i)}(t)$], and small grain mass [$m_{S(i)}(t)$] in the i th gas particle is written as (following equations 1, 3, and 4 in [Hirashita 2015](#))

$$\frac{dm_{g(i)}(t)}{dt} = -\psi_i + \frac{dm_{g(i)}^{\text{return}}}{dt}, \quad (\text{A1})$$

$$\frac{dm_{L(i)}(t)}{dt} = -\mathcal{D}_{L(i)}\psi_i \quad (\text{A2})$$

$$-\left(\frac{m_{L(i)}(t)}{\tau_{\text{sh}}} - \frac{m_{S(i)}(t)}{\tau_{\text{co}}}\right) - \frac{m_{L(i)}(t)}{\tau_{\text{sp}}(a_L)} + \left[\frac{dm_{L(i)}(t)}{dt}\right]_{\text{Source}} - \left[\frac{dm_{L(i)}(t)}{dt}\right]_{\text{SNe}}, \quad (\text{A3})$$

$$\frac{dm_{S(i)}(t)}{dt} = -\mathcal{D}_{S(i)}\psi_i \quad (\text{A4})$$

$$\left(\frac{m_{L(i)}(t)}{\tau_{\text{sh}}} - \frac{m_{S(i)}(t)}{\tau_{\text{co}}} + \frac{m_{S(i)}(t)}{\tau_{\text{acc}}}\right) - \frac{m_{S(i)}(t)}{\tau_{\text{sp}}(a_S)} - \left[\frac{dm_{S(i)}(t)}{dt}\right]_{\text{SNe}}, \quad (\text{A5})$$

where ψ_i is the star formation rate of the i th gas particle. The time derivatives of dust mass can be converted to those of dust-to-gas ratio using the following relation between $dm_{L/S(i)}/dt$ and $d\mathcal{D}_{L/S(i)}/dt$:

$$m_{g(i)} \frac{d\mathcal{D}_{L/S(i)}}{dt} = m_{g(i)} \frac{d}{dt} \left(\frac{m_{L/S(i)}}{m_{g(i)}} \right) \quad (\text{A6})$$

$$= \frac{dm_{L/S(i)}}{dt} - \mathcal{D}_{L/S(i)} \frac{dm_{g(i)}}{dt} \quad (\text{A7})$$

$$= \frac{dm_{L/S(i)}}{dt} + \mathcal{D}_{L/S(i)}\psi - \mathcal{D}_{L/S(i)} \frac{dm_{g(i)}^{\text{return}}}{dt}. \quad (\text{A8})$$

By using this relation and rewriting $[dm_{L/S(i)}/dt]_{\text{Source}}/m_{g(i)} = [d\mathcal{D}_{L/S(i)}/dt]_{\text{Source}}$ and $[dm_{L/S(i)}/dt]_{\text{SNe}}/m_{g(i)} = [d\mathcal{D}_{L/S(i)}/dt]_{\text{SNe}}$, we obtain equations (5) and (6). The astration terms do not appear in these equations because astration does not change the dust-to-gas ratio (i.e. dust and gas are both consumed

without changing the dust-to-gas ratio of the remaining gas).

This paper has been typeset from a $\text{\TeX}/\text{\LaTeX}$ file prepared by the author.